

Three-dimensional finite-element modelling of Earth's viscoelastic deformation: effects of lateral variations in lithospheric thickness

Shijie Zhong, Archie Paulson and John Wahr*

Department of Physics, University of Colorado, Boulder, CO 80309, USA. E-mail: szhong@anquetil.colorado.edu

Accepted 2003 July 10. Received 2003 June 25; in original form 2002 July 26

SUMMARY

We have developed a 3-D spherical finite-element model to study the dynamic response to surface loads of a self-gravitating and incompressible Earth with 3-D viscoelastic structure. We have forced our model with the ICE-3G deglaciation history of Tushingham & Peltier to study the effects of laterally varying lithospheric thickness on observations of post-glacial rebound (PGR). The laterally varying lithospheric thicknesses are derived from estimates of the thermal structure of the oceanic lithosphere and from elastic thicknesses on continents as estimated from studies of long-term geological loads. Our calculations show that the effects of lithospheric structure on the relative sea level change (RSLC) depend on the locations of the observation sites and on the size of loads. The RSLC at the centre of the North American ice sheet is significantly less sensitive to lithospheric thickness, compared with the RSLC at the centre of the Fennoscandian ice sheet. At the peripheral bulges the RSLC tends to be more sensitive to lithospheric thickness. The RSLC is controlled by local lithospheric thickness. The RSLC at a given location, as predicted using models with laterally varying lithospheric thickness, can be reproduced using a 1-D model with a uniform lithospheric thickness equal to the local lithospheric thickness. Coupled with efficient parallel computing, we believe that the finite-element model that we present here can be used to address a variety of viscoelastic deformation problems in geodynamics.

Key words: finite-element models, lithospheric thickness variations, mantle viscosity, post-glacial rebound.

1 INTRODUCTION

An understanding of mantle viscosity is fundamental to many aspects of geodynamics including the thermal evolution of the Earth, mantle convection and plate tectonics. Over the last three decades, it has been demonstrated that mantle viscosity can be constrained by modelling the long-wavelength non-hydrostatic geoid (Hager & Richards 1989) and post-glacial rebound (referred to as PGR hereafter) data (Cathles 1975; Peltier 1976). Recent studies indicate that the mantle viscosity structure inferred from modelling the geoid and PGR are similar, with the lower mantle being perhaps as much as one to two orders of magnitude more viscous than the upper mantle and transition zone (Hager & Richards 1989; Lambeck *et al.* 1990; Han & Wahr 1995; Forte & Mitrova 1996; Mitrova & Forte 1997; Simons & Hager 1997), although a smaller increase of viscosity in the lower mantle has also been proposed (Peltier 1998). This suggests that the mantle responds in a similar fashion to loads

at different timescales (i.e. ice loads at timescales of $\sim 10^4$ yr and mantle convection at timescales $> 10^6$ yr).

Each of these two methods of constraining the viscosity (i.e. modelling the geoid and using PGR data) has advantages and disadvantages. The rebound signal tends to be somewhat less sensitive to deep mantle structure than the long-wavelength geoid, due to the relatively small size of the ice sheets (e.g. Peltier 1998). However, the geoid can constrain only the relative viscosity structure, because it does not contain information on the time dependence (Mitrova & Forte 1997). The temporal and spatial patterns of PGR, on the other hand, are sensitive to both the relative viscosity structure and the absolute value of viscosity.

Constraints on mantle viscosity are obtained by comparing the PGR observations against model predictions of the Earth's response to the ice load removal (i.e. a deglaciation history). At timescales appropriate for PGR, the Earth responds to loads as a viscoelastic medium, rather than as a purely viscous body. Using the correspondence principle, classical elastodynamic models can be extended to determine the viscoelastic response of the Earth to surface loads (e.g. Peltier 1976). In the usual elastodynamic models for loading of a spherically symmetric Earth, the solution scalars are expanded as sums of spherical harmonics and the radially dependent

*Also at: Cooperative Institute for Research in Environmental Sciences University of Colorado.

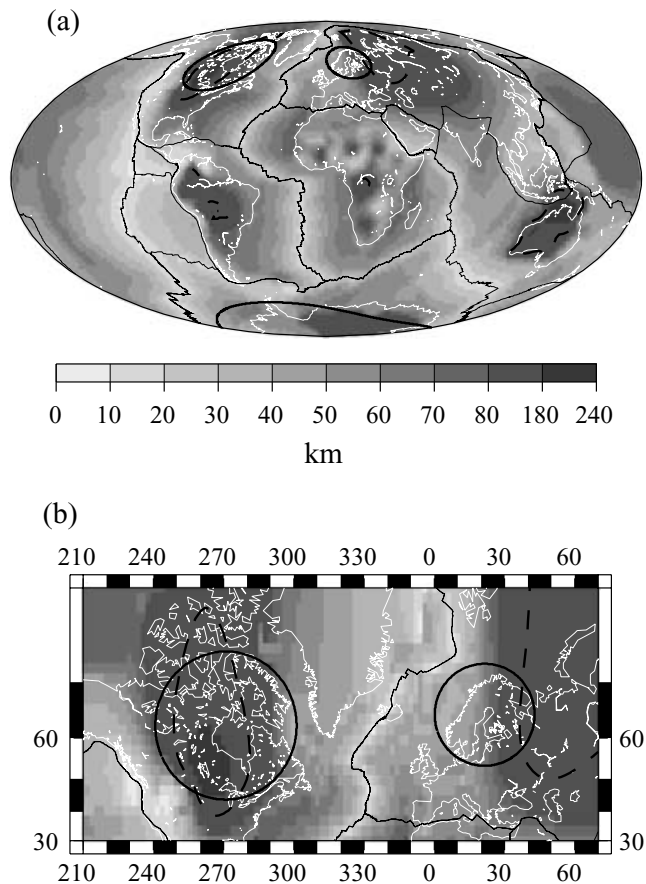


Figure 1. Lithospheric thickness variations on a global scale (a) and for North America and Europe (b). The solid black lines mark major plate boundaries. The dashed black lines are contours for 120 km thick lithosphere. The lithospheric thickness is modified from Watts (2001).

coefficients of the spherical harmonics are determined by solving a set of ordinary differential equations over radius. This type of analysis has been used extensively in modelling PGR (e.g. Wu & Peltier 1982; Mitrović & Peltier 1991; Peltier 1998). However, this is a particularly useful method only in cases where the Earth's viscoelastic structure depends only on the radius, because in that case the differential equations for different harmonic coefficients are completely decoupled from one another. When lateral variations in viscoelastic structure are present, the Earth's response to a single harmonic load consists of many additional harmonics (e.g. Kaufmann & Wolf 1999; Wu 2002a). This generally precludes the use of this method for an Earth with a fully 3-D mantle and lithospheric structure (e.g. Fig. 1 for laterally varying lithospheric thickness). For this reason, most studies of PGR assume a spherically symmetric (i.e. 1-D) viscoelastic structure, including a uniform lithospheric thickness.

A number of methods have been used to model viscoelastic deformation in the presence of lateral viscosity variations. These include perturbation methods (Tromp & Mitrović 2000), and numerical methods (Sabadini *et al.* 1986; Gasperini & Sabadini 1989; Wu 1992, 1993, 2002b; Wu *et al.* 1998; Giunchi *et al.* 1997; Kaufmann *et al.* 1997; Kaufmann & Wu 1998, 2002; Martinec 1999, 2000; Martinec *et al.* 2001). Among these numerical methods, only Wu (2002b) with a finite-element method, and Martinec (1999, 2000) with a spectral method, included a fully 3-D spherical geometry. The other studies employed Cartesian or axisymmetric models. Wu (2002b), which is the only study that we are aware of where a fully

3-D method has actually been used to compute the effects of laterally varying viscosity, adopted a commercial finite-element software for the PGR studies, which without parallel computing technology is useful mostly for very long-wavelength problems. Martinec (1999, 2000) presented a spectral finite-difference/finite-element method but did not investigate the effects of laterally varying structure.

Although the effects of laterally varying viscosity including non-Newtonian mantle viscosity are not yet well understood, some general characteristics have been identified. For example, Sabadini *et al.* (1986) showed that the rebound at the margins of a formerly glaciated area is sensitive to lithospheric thickness variations; much more so than is the rebound near the centre. With similar 2-D models, Kaufmann *et al.* (1997) demonstrated that effects of lithospheric thickness variations can be resolved with models with different uniform lithospheric thicknesses. Gasperini & Sabadini (1989) found that lateral variations in upper-mantle viscosity of one to two orders of magnitude and with wavelengths comparable to the horizontal dimension of ice loads could significantly affect the rebound at the load centre, consistent with other studies from 2-D and 3-D regional models (Wu *et al.* 1998; Kaufmann & Wu 1998; Kaufmann *et al.* 1997, 2000). Giunchi *et al.* (1997) suggested that continental roots and lateral variations in viscosity in the asthenosphere could have important effects on present-day horizontal surface displacements (also see Ni & Wu 1998; Martinec *et al.* 2001). Wu (1992, 1993, 1995, 2002c) examined whether a non-Newtonian mantle rheology is compatible with PGR data. He concluded that PGR data did not support a non-Newtonian rheology that would result in much faster relaxation than the observations for reasonable ambient tectonic stress.

We have formulated a robust and efficient 3-D spherical finite-element model for studies of viscoelastic deformation for Earth with 3-D viscoelastic structure. With this new finite-element model, we have investigated the effects of laterally varying mantle and lithospheric structure on the PGR. In this paper we will present our numerical formulation and benchmarks. We will focus on the role of laterally varying lithospheric thickness, while the effects of lateral variations in mantle viscosity will be presented in other papers. At the current stage, we do not intend to invert for 3-D viscosity structure with PGR observations. Our general philosophy is to understand the effects of laterally varying structure on the observables and to examine to what extent PGR from 3-D mantle structure can be modelled with 1-D mantle structure.

We organize the paper as follows. First, we define the mathematical models that describe viscoelastic deformation of an Earth with a fully 3-D structure. Secondly, we describe numerical methods that are employed to solve the equations of motion. Thirdly, we demonstrate the accuracy of our numerical methods by comparing our solutions against semi-analytic solutions. Fourthly, we examine the effects of lateral variations in lithospheric thickness. The final section includes a discussion and conclusions.

2 PHYSICAL MODELS FOR VISCOELASTIC DEFORMATION

2.1 Governing equations

We assume an incompressible Earth with self-gravitation. Our models only include a viscoelastic mantle (Fig. 2a) that overlies an inviscid fluid core. The response of a self-gravitating and incompressible mantle to surface loads can be described by the governing equations of mass and momentum and the equation for the gravitational

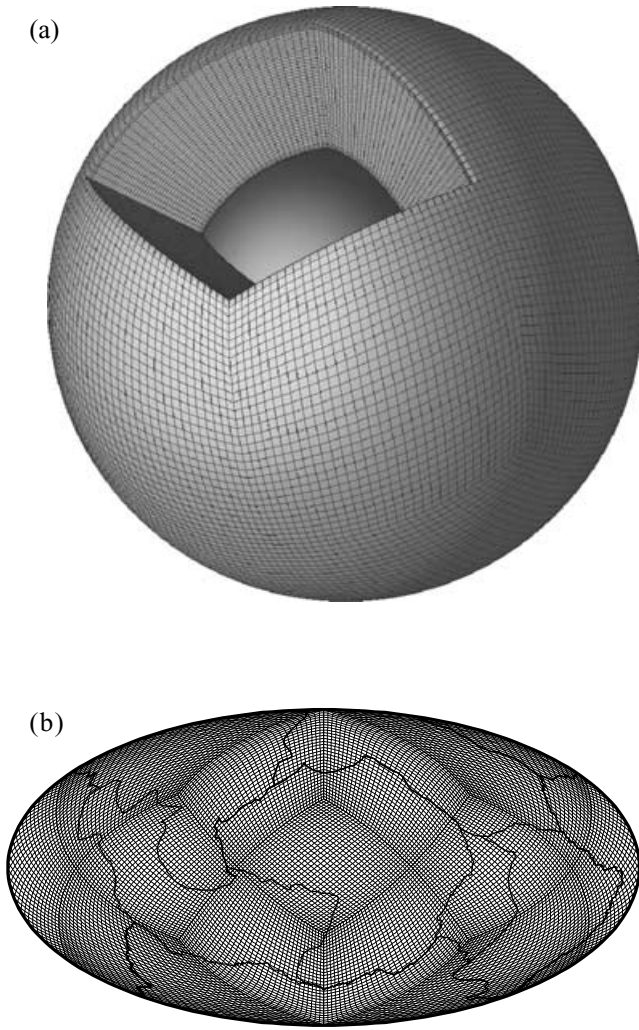


Figure 2. Finite element grids for a 3-D view (a) and a plan view (b).

perturbation (Wu & Peltier 1982):

$$u_{i,i} = 0, \quad (1)$$

$$\sigma_{ij,j} + \rho_0 \phi_{,i} - \rho_1 g_i - (\rho_0 g u_r)_{,i} = 0, \quad (2)$$

$$\phi_{,ii} = -4\pi G \rho_1, \quad (3)$$

where u_i is the displacement, σ_{ij} is the stress tensor, ρ_0 and g_i are the unperturbed density and gravitational acceleration with magnitude of $g = \sqrt{g_i g_i}$, u_r is the radial component of the displacement, ϕ is the perturbation of the gravitational potential and G is the gravitational constant. We use a notation such that $A_{,i}$ represents the derivative of variable A with respect to x_i , and repeated indices indicate summation over those indices. ρ_1 in eqs (2) and (3) is the Eulerian density perturbation (Wu & Peltier 1982; Tromp & Mitrović 1999), and given by $\rho_1 = -u_i \rho_{0,i}$ in an incompressible medium.

2.2 Boundary conditions

We consider surface loads that produce pressure $\sigma(t, \theta, \varphi)$ on the surface. The surface loads may depend on time t , colatitude θ and

longitude φ (e.g. a model of glaciation history). The boundary conditions on surface traction at the surface and core–mantle boundary (CMB) are given by

$$\sigma_{ij} n_j = -\sigma(t, \theta, \varphi) n_i, \quad \text{for } r = r_s, \quad (4)$$

$$\sigma_{ij} n_j = (-\rho_c \phi + u_r \rho_c g) n_i, \quad \text{for } r = r_b, \quad (5)$$

where ρ_c is the core density that we assume to be uniform throughout the core, and r_s and r_b are the radii of the surface and CMB, respectively; n_i represents the normal vector of the surface or CMB, and σ_{ij} is the stress tensor on the mantle side of the boundary. The boundary condition (5) is derived from the requirement that the normal stress be continuous across the CMB, and applying the equation of motion (2) to the core and using the fact that $\sigma_{ij} = -P \delta_{ij}$ in a fluid. Neither the surface nor CMB supports shear stress. The radial stress at the CMB results from self-gravitation. With these boundary conditions, both the surface and CMB can deform dynamically.

The boundary conditions for eq. (3) are given by

$$\phi(r^+) = \phi(r^-), \quad \text{for } r = r_s \quad \text{and} \quad r = r_b, \quad (6)$$

$$n_i \phi_{,i}(r^+) + 4\pi G \rho(r^+) n_i u_i(r) = n_i \phi_{,i}(r^-) + 4\pi G \rho(r^-) n_i u_i(r), \quad \text{for } r = r_s \quad \text{and} \quad r = r_b, \quad (7)$$

where $\rho(r^+) = 0$ at the outer surface.

2.3 Mechanical properties

The rheological equations for an incompressible viscoelastic medium (i.e. a Maxwell body) can be written in terms of viscous and elastic deformation,

$$\dot{\varepsilon}_{ij}^v = \frac{1}{2\eta} (\sigma_{ij} + P \delta_{ij}), \quad (8)$$

$$\varepsilon_{ij}^e = \frac{1}{2\mu} (\sigma_{ij} + P \delta_{ij}), \quad (9)$$

where μ and η are the shear modulus and viscosity, respectively, P is the pressure, ε_{ij}^v and ε_{ij}^e are the strain tensors for viscous and elastic deformation, δ_{ij} is the Kronecker delta; and the dot over ε_{ij}^v denotes the time derivative. We define the total strain tensor as

$$\varepsilon_{ij} = \varepsilon_{ij}^v + \varepsilon_{ij}^e = \left(\frac{\partial u_i}{\partial x_j} + \frac{\partial u_j}{\partial x_i} \right) / 2. \quad (10)$$

Adding eq. (8) to the time derivatives of eq. (9) leads to

$$\sigma_{ij} + \frac{\eta}{\mu} \dot{\sigma}_{ij} = - \left(P + \frac{\eta}{\mu} \dot{P} \right) \delta_{ij} + 2\eta \dot{\varepsilon}_{ij}. \quad (11)$$

Our models may include fully 3-D structure for the shear modulus μ and viscosity η , but we will consider only layered density structures in which the density is constant within each layer. In this study, we will assume a uniform mantle density $\rho_0 = \text{constant}$. With this assumption, the Eulerian density perturbation ρ_1 vanishes from eqs (2) and (3).

3 NUMERICAL ANALYSIS OF VISCOELASTIC DEFORMATION

Given that we have previously developed spherical finite-element models for purely viscous mantle flows (Zhong *et al.* 2000), our basic strategy here is to reformulate our viscoelastic problem so

that it is similar to those encountered in studies of mantle convection. The resulting equations can then be solved with similar finite-element methods. The key difference between viscous deformation and viscoelastic deformation is that the rheological equation depends on time for viscoelastic deformation (e.g. eq. 11) but not for viscous deformation. Other significant differences include the full coupling between boundary deformation and self-gravitation (i.e. eqs 3 and 7). As a result of these differences, some special numerical treatments are required, and we discuss them as follows.

3.1 An incremental displacement formulation

The equations in Section 2 use total displacements u_i and strains ε_{ij} . However, it is more convenient to use a formulation with incremental displacements and strains, which will be clear after we discretize the rheological equation in the next subsection. Let u_i^n and u_i^{n-1} be displacements at times t and $t - \Delta t$, respectively, where the superscripts n and $n - 1$ are for time steps corresponding to times t and $t - \Delta t$. An incremental displacement v_i^n and incremental strain $\Delta\varepsilon_{ij}^n$ may be defined as

$$v_i^n = u_i^n - u_i^{n-1}, \quad (12)$$

$$\Delta\varepsilon_{ij}^n = \left(\frac{\partial v_i^n}{\partial x_j} + \frac{\partial v_j^n}{\partial x_i} \right) / 2. \quad (13)$$

With incremental displacements, eq. (1) can be expressed as

$$v_{i,i} = 0, \quad (14)$$

where the time step index has been dropped, implying that incompressibility is maintained at all times.

3.2 Discretization of the rheological equation

We may discretize the rheological eq. (11) by integrating it over a time increment Δt from $t - \Delta t$ to t with the second-order accurate trapezoid rule,

$$\sigma_{ij}^n = -P^n \delta_{ij} + \frac{2\eta}{\alpha + \Delta t/2} \Delta\varepsilon_{ij}^n + \frac{\alpha - \Delta t/2}{\alpha + \Delta t/2} (\sigma_{ij}^{n-1} + P^{n-1} \delta_{ij}), \quad (15)$$

where superscripts n and $n - 1$ indicate the time steps, and $\alpha = \eta/\mu$. The total strains are no longer present in eq. (15), which includes only the incremental strain $\Delta\varepsilon_{ij}^n$. The last term in eq. (15) is associated with stresses from the previous time step, and reflects the dependence of the deformation on its history. We use the stresses at time step $n - 1$ to define the pre-stress

$$\tau_{ij}^{\text{pre}} = \frac{\alpha - \Delta t/2}{\alpha + \Delta t/2} (\sigma_{ij}^{n-1} + P^{n-1} \delta_{ij}). \quad (16)$$

Because τ_{ij}^{pre} depends on the sum of total stress and pressure, eq. (15) implies that τ_{ij}^{pre} depends only on deviatoric stresses. eq. (16) also suggests that to adequately account for the effects of the pre-stress Δt cannot be too large. For example, for $\Delta t = 2\alpha$, the pre-stress terms are uniformly zero, implying that no pre-stress effects are considered. With the pre-stress, we may rewrite eq. (15) as

$$\sigma_{ij} = -P \delta_{ij} + 2\tilde{\eta} \Delta\varepsilon_{ij} + \tau_{ij}^{\text{pre}}, \quad (17)$$

where we have omitted the time step indices, and $\tilde{\eta} = \eta/(\alpha + \Delta t/2)$. Eq. (17) is identical to rheological equations used for viscous flow except for the pre-stress term.

3.2.1 Solutions for the perturbed gravitational potential

Because our models assume a constant density within the mantle, only three sources of mass anomalies contribute to the perturbed gravitational potential ϕ . They are associated with surface loads and topographic variations at the surface and CMB. Let $\Delta\rho_b$ and $\Delta\rho_s$ be the density increases across the CMB and surface, respectively, $u_{lm}^b(t)$ and $u_{lm}^s(t)$ be the time-dependent radial displacements at these two boundaries, and $\sigma_{lm}(t)/g$ be the surface mass density associated with surface loads at spherical harmonic degree l and order m . With the radial displacements and surface mass density represented in a spherical harmonic domain, the solution to eq. (3) can be expressed as

$$\phi_{lm}(r, t) = \frac{4\pi G}{2l+1} \left\{ r_b \left(\frac{r_b}{r} \right)^{l+1} \Delta\rho_b u_{lm}^b(t) + r_s \left(\frac{r}{r_s} \right)^l \left[\Delta\rho_s u_{lm}^s(t) + \frac{\sigma_{lm}(t)}{g} \right] \right\} \quad (18)$$

for every l and m .

Note that radial displacements $u_{lm}^b(t)$ and $u_{lm}^s(t)$ in eq. (18) are solutions from eqs (1) and (2) that in turn depend on ϕ in eq. (18). For any given time t , we may introduce incremental radial displacements $v_{lm}^b = u_{lm}^b(t) - U_{lm}^b$ and $v_{lm}^s = u_{lm}^s(t) - U_{lm}^s$, where U_{lm}^s and U_{lm}^b are the surface and CMB radial displacements at time $t - \Delta t$. Eq. (18) may be rewritten as

$$\phi_{lm}(r, t) = \frac{4\pi G}{2l+1} \left\{ r_b \left(\frac{r_b}{r} \right)^{l+1} \Delta\rho_b (v_{lm}^b + U_{lm}^b) + r_s \left(\frac{r}{r_s} \right)^l \left[\Delta\rho_s (v_{lm}^s + U_{lm}^s) + \frac{\sigma_{lm}(t)}{g} \right] \right\}. \quad (19)$$

In eq. (19), the unknowns that the potential ϕ_{lm} depends on at time t are the incremental displacements v_{lm}^s and v_{lm}^b . We recover the potential $\phi(r, \theta, \varphi, t)$ in the spatial domain by adding up the contributions ϕ_{lm} , from all the harmonics. We express $\phi(r, \theta, \varphi, t)$ as

$$\phi(r, \theta, \varphi, t) = \Phi(r, \theta, \varphi) + \delta\phi(v_{rs}, v_{rb}), \quad (20)$$

where $\Phi(r, \theta, \varphi)$ represents the potential from radial displacements at the density interfaces from the previous time step and surface loads, and $\delta\phi(v_{rs}, v_{rb})$ is the potential from the unknown incremental displacements at the current time step.

3.3 Discretization of the momentum equation

We use a primitive variable formulation that solves for the pressure and incremental displacement. With a vanishing Eulerian density perturbation, we may rewrite the momentum equation as

$$(\sigma_{ij} + \rho_0 \phi \delta_{ij} - \rho_0 g u_r \delta_{ij})_{,j} = 0. \quad (21)$$

Multiplying eq. (21) by a displacement weighting function w_i , integrating over a volume (e.g. the mantle) V that is bounded by surface S (Hughes 1987), and substituting the rheological eq. (17) into the integral, lead to

$$\begin{aligned} & \int_V w_{i,j} [-(P - \rho_0 \phi + \rho_0 g u_r) \delta_{ij} + \tilde{\eta} (v_{i,j} + v_{j,i})] dV \\ &= - \int_V w_{i,j} \tau_{ij}^{\text{pre}} dV + \int_S w_i (\sigma_{ij} + \rho_0 \phi \delta_{ij} - \rho_0 g u_r \delta_{ij}) n_j dS, \end{aligned} \quad (22)$$

where n_j represents the normal vector of surface S . We define an effective pressure $\tilde{P} = P - \rho_0 \phi + \rho_0 g u_r$ and use it, instead of P , as an unknown variable in our solution. Substituting boundary conditions (4) and (5) and the perturbed potential (20) into eq. (22),

Table 1. Model parameters.

Parameter	Value
Radius of Earth, r_s	6.3700×10^6 m
Radius of CMB, r_b	3.5035×10^6 m
Mantle shear modulus, μ	1.4305×10^{11} Pa
Mantle density [†] , ρ_0	5500 kg m^{-3} (4400 kg m^{-3})
Density difference across CMB, $\Delta\rho_b$	5425 kg m^{-3}
Gravitational acceleration, g	9.8 m s^{-2}

[†]Mantle density for the Heaviside loading models is different from that for the models with ICE-3G loads, and the latter is in parentheses.

and separating S into S_s and S_b where S_s and S_b represent the surface and CMB, we have

$$\begin{aligned}
& \int_V w_{i,j} [-\tilde{P}\delta_{ij} + \tilde{\eta}(v_{i,j} + v_{j,i})] dV + \int_{S_s} w_i \Delta\rho_s g v_r \delta_{ir} dS \\
& + \int_{S_b} w_i \Delta\rho_b g v_r \delta_{ir} dS \\
& = - \int w_{i,j} \tau_{ij}^{\text{pre}} dV + \int_{S_s} w_i (\rho_0 \Phi - \Delta\rho_s g U_{rs} - \sigma) \delta_{ir} dS \\
& + \int_{S_b} w_i (\Delta\rho_b \Phi - \Delta\rho_b g U_{rb}) \delta_{ir} dS + \int_{S_s} w_i \rho_0 \delta\phi \delta_{ir} dS \\
& + \int_{S_b} w_i \Delta\rho_b \delta\phi \delta_{ir} dS, \tag{23}
\end{aligned}$$

where U_{rs} and U_{rb} are the radial displacements at the surface and CMB at the previous time step.

For a given finite-element grid, the momentum and continuity equations (i.e. eqs 23 and 14) may be written as a system of matrix equations for \tilde{P} and v_i (Hughes 1987). We use brick elements each with a constant pressure node at its centre and eight nodes at its cor-

ners for displacement (e.g. Moresi & Gurnis 1996), and the same finite-element grid as in Zhong *et al.* (2000) for the mantle (Fig. 2). The second and third integrals on the left-hand side of eq. (23) represent additional terms to the ordinary stiffness matrix. The first three integrals on the right-hand side of eq. (23) are known through either boundary conditions (e.g. surface loads σ) or calculations from previous time steps (e.g. Φ , τ_{ij}^{pre} , U_{rs} and U_{rb}). However, the last two integrals are associated with the incremental potential $\delta\phi$, which depends on the unknown incremental displacements, as indicated in eq. (20). The next subsection discusses the strategy we employ to overcome this difficulty.

3.4 Matrix equations and their solutions

The matrix equations for \tilde{P} and v_i from eqs (14) and (23) can be written as (Hughes 1987; Moresi & Solomatov 1995)

$$A^T V = 0, \tag{24}$$

$$K V + A P = F_0 + F(V), \tag{25}$$

where K is the stiffness matrix, A is the gradient matrix, the superscript T represents the transpose, V and P are vectors for the unknowns v_i and \tilde{P} , respectively, F_0 is the force vector that is derived from the first three integrals of the right-hand side of (23); and $F(V)$ is derived from the last two integrals of eq. (23). $F(V)$ depends on the incremental potential $\delta\phi$ and is therefore dependent on the incremental displacement vector V .

For force terms with no dependence on V , matrix eqs (24) and (25) can be solved with the Uzawa algorithm coupled with multigrid based methods (e.g. Moresi & Solomatov 1995; Zhong *et al.* 2000). For $F(V)$, we introduce iterative procedures summarized as follows. For a given time step, (1) make a guess for $V = V_0$ and compute $F(V_0)$; (2) solve eqs (24) and (25) with the guessed force terms for

Table 2. Amplitude and dispersion errors for cases with heaviside function loading.

Case	Vis [†]	(l, m)	Δt^\ddagger	SG*	Surface		CMB	
					ε_a (per cent)	ε_d (per cent)	ε_a (per cent)	ε_d (per cent)
A1	I	(2,0)	0.2	1	0.07	0.03	0.07	0.04
A2	I	(4,0)	0.2	1	0.14	0.14	0.24	0.29
A3	I	(8,0)	0.2	1	0.59	0.08	1.47	1.15
A4	W	(2,0)	0.2	3	0.21	0.05	0.39	0.06
A5	W	(4,0)	0.2	3	0.29	0.18	0.72	0.46
A6	W	(8,0)	0.2	3	0.41	0.17	0.16	1.46
A7	I	(2,0)	0.2	2	1.12	0.05	1.44	0.07
A8	I	(4,0)	0.2	2	0.52	0.17	0.46	0.29
A9	I	(8,0)	0.2	2	0.85	0.12	1.56	1.18
A10	I	(2,0)	0.2	3	0.21	0.03	0.22	0.05
A11	I	(4,0)	0.2	3	0.12	0.17	0.31	0.29
A12	I	(8,0)	0.2	3	0.63	0.12	1.30	1.15
A13	I	(2,0)	0.1	3	0.08	0.03	0.13	0.05
A14	I	(2,0)	0.4	3	0.50	0.04	0.62	0.06
A15	I	(2,1)	0.2	3	0.18	0.03	0.21	0.04
A16	I	(4,2)	0.2	3	0.11	0.07	0.24	0.06
A17	I	(8,4)	0.2	3	0.61	0.09	1.32	2.33

[†]Models I and W are for an isoviscous mantle and for a mantle with a weak upper mantle (3 per cent), respectively. Both types of models have a 100 km thick elastic plate.

[‡]The time step, Δt , for the numerical models is measured with Maxwell time η/μ , where η is the lower mantle viscosity.

*Three implementation strategies for including the incremental potential are used. Type 1 uses the full iterative approach, while in types 2 and 3 the incremental potential is taken from the last time step and interpolated from the last two time steps, respectively.

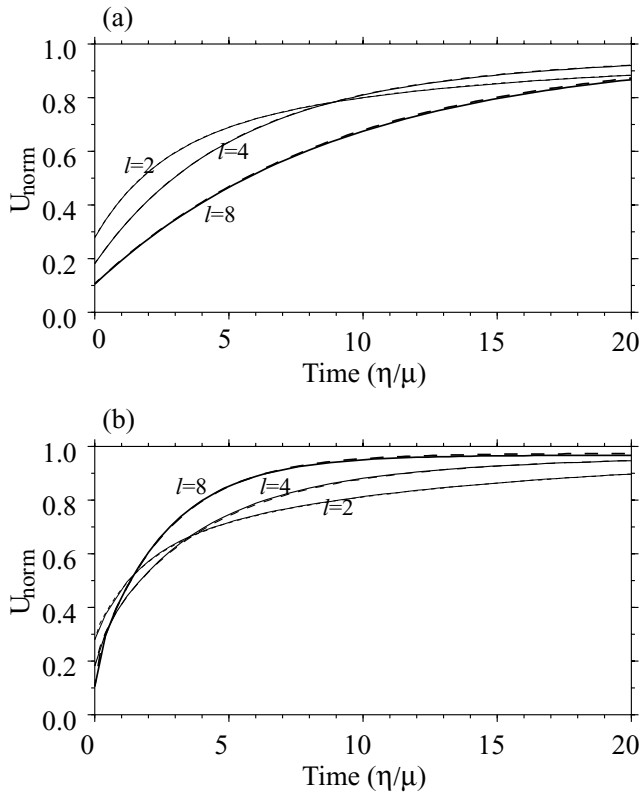


Figure 3. Time-dependent vertical displacement from semi-analytic solutions (dashed lines) and from the finite-element method (solid lines), for an isoviscous mantle (a), and for a stratified mantle with a weak upper mantle (b), in response to single harmonic ($l_0 = 2, 4$ and 8) Heaviside function loads. Error analyses are presented in Table 2. U_{norm} represents the displacement normalized by $1/(\rho_0 g)$.

V_n and P_n ; (3) let $V = V_n$ and repeat steps (1) and (2) until V_n and P_n converge. (4) $V = V_n$ and $P = P_n$ are the solutions for this time step.

This iterative method is computationally expensive. An alternative approach is to linearize this procedure by simply using V from the previous time step or by interpolating V from the previous two time steps. The linearized approach requires full iteration only for the first one or two time steps.

4 COMPARISONS WITH SEMI-ANALYTIC SOLUTIONS

To assess the performance of our numerical algorithm, we use it to generate solutions for spherically symmetric Earth models, and compare them with predictions from standard semi-analytic methods commonly used to address spherically symmetric problems. Comparisons are presented here for two types of problems. One uses simple loads (i.e. a single harmonic load with a Heaviside function loading history), and the other uses the realistic ice loading model ICE-3G (Tushingham & Peltier 1991).

4.1 Single harmonic loads with heaviside function loading history

We use unit surface loads

$$\sigma(t, \theta, \varphi) = H(t)Y_{l_0 m_0}(\theta, \varphi), \quad (26)$$

where $H(t)$ is the Heaviside function (i.e. $H(t)$ is 1 for $t \geq 0$ and 0 for $t < 0$); $Y_{l_0 m_0}(\theta, \varphi)$ is the spherical harmonic function for degree l_0 and order m_0 .

The unperturbed density, shear modulus and gravitational acceleration throughout the mantle are each assumed to be uniform (Table 1). Mantle viscosity is assumed to depend only on radius. Two viscosity structures are investigated: (1) a 100 km thick plate

Table 3. Comparisons for cases with the ICE-3G.

Case	Vis [†]	Grid [‡]	Δt^* (yr)	Time (ka)	$\epsilon_{\text{rslc}}^{\#}$ (per cent)	ϵ_{rate} (per cent)	ϵ_{disp} (per cent)
B1	U	$48 \times 48 \times 48$	200 (100)	0	5.37	5.69	6.49
				-10	4.30	3.05	3.21
				-28	2.95	2.30	2.52
B2	U	$48 \times 48 \times 48$	100 (50)	0	4.38	4.67	6.52
				-10	3.53	1.95	2.68
				-28	2.99	2.34	2.38
B3	U	$80 \times 80 \times 40$	200 (100)	0	3.42	3.38	4.95
				-10	3.32	1.94	2.20
				-28	1.30	0.61	0.64
B4	U	$80 \times 80 \times 40$	200 (25)	0	1.49	1.74	3.38
				-10	2.43	0.70	0.85
				-28	1.30	0.61	0.64
B5	W	$80 \times 80 \times 40$	200 (25)	0	0.68	0.80	1.30
				-10	2.86	1.44	0.63
				-28	1.39	0.69	0.78

[†]Two types of viscosity structures, U and W. For type U, viscosities in the upper and lower mantles are 10^{21} Pa s and 2×10^{21} Pa s, respectively. For type W, viscosities in the upper and lower mantles are 3×10^{20} and 10^{22} Pa s, respectively. For both types, a 120 km thick lithosphere is included.

[‡]Grid for each of the 12 blocks that divide the mantle (Fig. 2a). The last number is the number of elements in the radial direction, and the vertical resolution is refined in the upper mantle and lithosphere.

*Time increment during glaciation is larger than that for post-glaciation. The numbers in parentheses are for post-glaciation.

[#]Errors are computed globally for RSLC, vertical rate, and vertical displacement for each of three time steps: $t = 0$ (i.e. present day), $t = -10$ and -28 ka.

overlying a constant viscosity mantle and (2) a 100 km thick plate overlying an upper mantle with a viscosity that is 3 per cent of that for the lower mantle.

For viscoelastic loading problems with such mechanical structures, semi-analytic solutions can be obtained. Our semi-analytic solutions are obtained from methods developed in Zhong & Zuber (2000) and Wahr *et al.* (2001). The analytic method by Zhong & Zuber (2000) is based on an Eulerian formulation solved using the Laplacian transform techniques, while Wahr *et al.* (2001) use the classical approach utilizing the correspondence principle. These two methods produce identical solutions.

For a Heaviside function loading on a viscoelastic medium, the initial response is purely elastic, and includes displacements at the surface and CMB and stress in the mantle. Subsequently, the mantle stress relaxes through viscous deformation. As the mantle stress relaxes with time, the surface loads with fixed amplitude (i.e. the Heaviside function loading) are increasingly supported by the surface and this causes the surface displacement to increase with time. The CMB displacement in general decreases with time. Eventually as the mantle stress relaxes completely, the surface must support the entire load. The time-dependent stress evolution has been well studied with various semi-analytic methods (e.g. Zhong & Zuber 2000).

Because the Earth is assumed to be spherically symmetric, the radial displacement at each boundary and over every shell of constant radius inside the Earth should have the same angular dependence as the load. This is a fundamental characteristic of the semi-analytic solutions. Therefore, the two measures we have adopted for assessing the numerical solutions in the case of $Y_{l_0 m_0}(\theta, \varphi)$ forcing are: (1) whether the l_0 and m_0 components of the numerical solutions agree with the same l_0 and m_0 components predicted by the semi-analytic method and (2) whether the other spherical harmonic components in the numerical solution are all close to zero. We have performed error analyses for our numerical solutions by comparing with semi-analytic solutions for 17 cases with different mantle viscosity structure and loading wavelengths, and the results are summarized in Table 2.

Our finite-element models use 48^3 elements for each of the 12 caps that dissect the spherical shell for the mantle (Zhong *et al.* 2000). Our numerical solutions agree with the semi-analytic solutions excellently for models with constant mantle viscosity and for models with a weak upper mantle, for three different wavelengths ($l_0 = 2, m_0 = 0$; $l_0 = 4, m_0 = 0$; $l_0 = 8, m_0 = 0$). Fig. 3, for example, compares the displacement fields from the numerical and semi-analytic solutions for the same harmonic degree and order used in the surface load. Table 2, cases A1–A6, summarizes the accuracy of the numerical solutions by showing the relative amplitude and dispersion errors. The amplitude error ε_a measures the deviation of the finite-element solution from the semi-analytic solution at the same harmonic of the loading l_0 and m_0 . The dispersion error ε_d measures the maximum amplitude of the other harmonics. These errors are defined as

$$\varepsilon_a = \frac{1}{T} \int_0^T \frac{|S_g(l_0, m_0, t) - S_n(l_0, m_0, t)|}{|S_g(l_0, m_0, t)|} dt, \quad (27)$$

$$\varepsilon_d = \max_{l, m, t} \left[\frac{|S_g(l_0, m_0, t) - S_n(l, m, t)|}{|S_g(l_0, m_0, t)|} \right], \quad (28)$$

for $l \neq l_0$ and $m \neq m_0$,

where $S_g(l, m, t)$ and $S_n(l, m, t)$ are the response at the harmonics l and m from the semi-analytic and finite-element methods, respectively, and T is the time duration for which we compute the errors

and is taken as $20\tau_0$ for all the cases ($\tau_0 = \eta/\mu$ is the Maxwell time and η here is the lower mantle viscosity).

The focus of these error analyses is to investigate the influence of the time increment Δt and of different treatments of the incremental gravitational potential, $\delta\phi$, when solving eqs (24) and (25). With the iterative approach for $\delta\phi$, as in cases A1–A3, the errors for the surface deformation are consistently smaller than 0.6 per cent (Table 2). However, if $\delta\phi$ is taken directly from the previous time step without iterations, a method that is computationally much more economic, the errors are markedly larger, especially at degree 2 for which self-gravitation is important (cases A7–A9 in Table 2). A good compromise is to take the interpolated $\delta\phi$ based on those from the previous two time steps as the current $\delta\phi$ in eq. (23). This interpolation method produces significantly better results without significantly increasing the computational cost (Table 2 for cases A10–A12).

For cases with the time increment Δt as large as $0.4\tau_0$ (cases A10, A13 and A14 in Table 2), the errors are consistently small. However, it seems that the effects of Δt depend on loading functions, as we will see in the next section. We have also computed cases with a longitudinal dependence (i.e. $m \neq 0$). The errors are consistent with the corresponding cases with $m = 0$ (compare cases A7–A9 with cases A15–A17 in Table 2). The errors for CMB displacement are

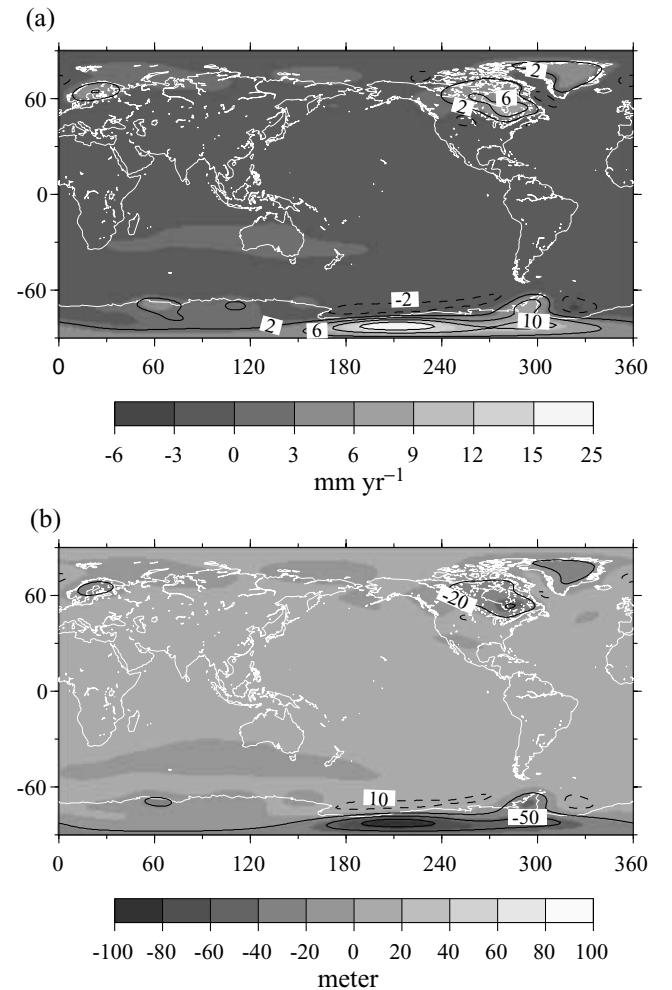


Figure 4. Present-day RSLC (a) and surface displacement (b) from case B4. The dashed contours are for negative values.

generally similar to those for surface displacement except for degree 8 loading (Table 2). The errors for degree 8 loading are primarily controlled by grid size.

4.2 ICE-3G loading model

We now compare the predicted vertical displacement (i.e. the displacement with respect to that at the beginning of the loading) and the vertical displacement rate at the surface, as well as the relative sea level change (i.e. RSLC), in response to the ICE-3G loading from our numerical models, with those predicted using a Green's function method (Wahr *et al.* 2001). Error analyses are performed for five cases with different mantle viscosity structure and temporal and spatial resolutions. The results are given in Table 3.

The ICE-3G model describes the temporal and spatial distribution of ice on the Earth's surface during the last 18 ka (Tushingham & Peltier 1991). We add a 90 ka, linearly increasing glaciation phase, to grow the ice sheets to their ICE-3G starting values. We expand the ice distribution as a sum of spherical harmonic components at

every time step, and use all terms with angular degree $l \leq 100$ (Wahr *et al.* 2001).

The RLSC is defined as the difference between the rate of change of the geoid and the rate of surface deformation (e.g. Peltier 1998). Although we consider the first 100 angular degrees for the ice loads, we only compute the geoid (or gravitational potential) up to degree and order 20 in the numerical models. Because the potential is computed in the spectral domain (see eq. 19) and because there are $2l + 1$ spherical harmonic coefficients for every l , the computational cost for the potential increases rapidly with the number of harmonics. The Green's function solutions for the potential, however, include all spherical harmonics up to $l = 100$.

Among the five cases in this section, cases B1–B4 include a 120 km thick elastic plate, an upper mantle with a viscosity of 10^{21} Pa s, and a lower mantle with a viscosity of 2×10^{21} Pa s. This viscosity structure was originally used by Tushingham & Peltier (1991) for the ICE-3G. In case B5, the viscosity contrast between the upper and lower mantle is larger (Table 3). The mantle density and shear modulus are 4400 kg m^{-3} and $1.4305 \times 10^{11} \text{ Pa}$ (Table 1). The incremental potential is computed using the interpolation method.

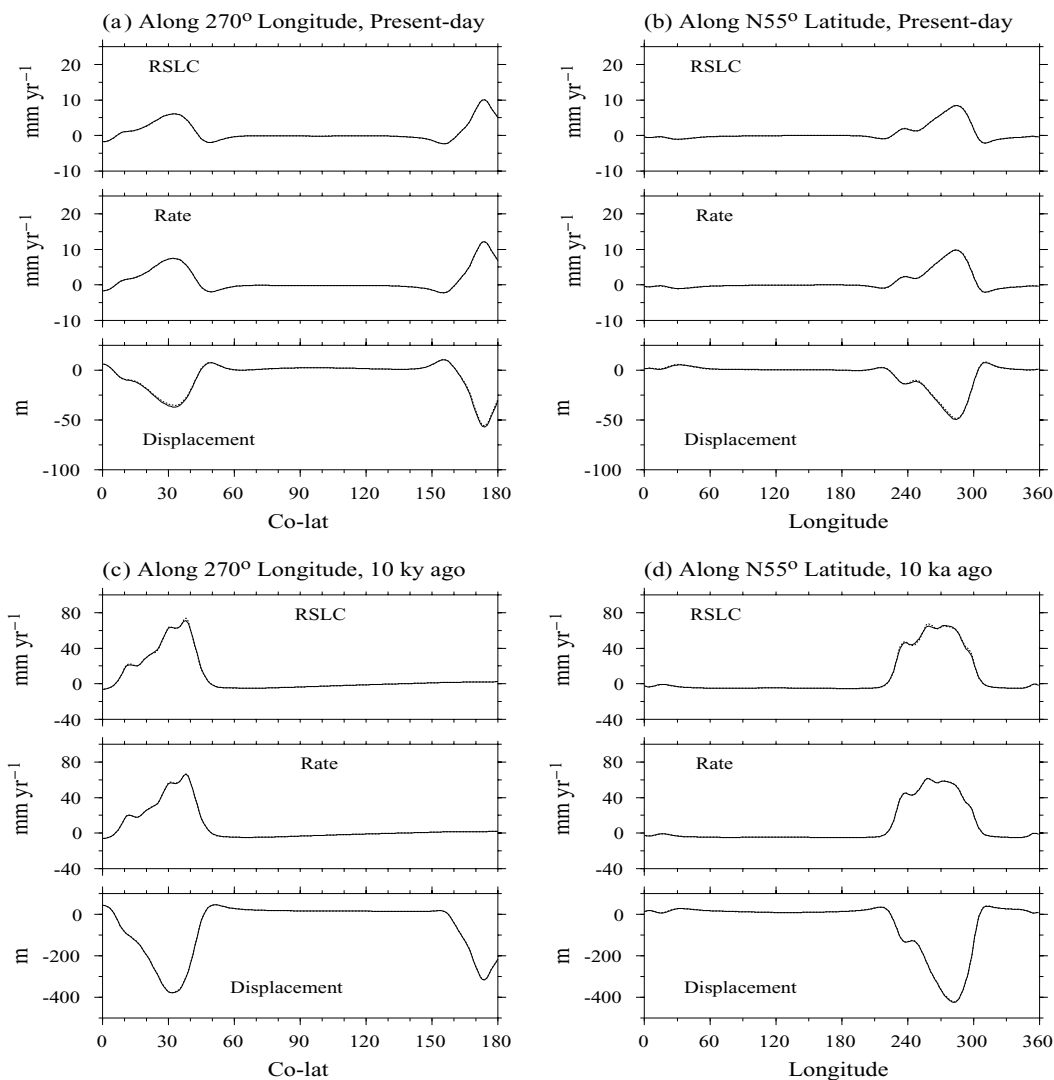


Figure 5. Responses from the finite-element method (solid lines) and the semi-analytic solutions (dashed lines) for case B4 along two profiles at two different times. Profiles along 270° longitude for the present day (a), 55° northern latitude for the present day (b), 270° longitude for $t = -10 \text{ ka}$ (c), and 55° northern latitude for $t = -10 \text{ ka}$ (d). In each of Figs 5(a)–(d), RSLC, vertical rate, and vertical displacement are shown in the top, middle and bottom panels, respectively. The results agree so well that the lines cannot be easily distinguished in most cases.

Cases with different temporal and spatial resolutions are computed to investigate their effects on the accuracy of our numerical models. Here we compute the global errors for vertical displacement, vertical displacement rate and RSLC at a given time t_0 . For example, the error for RSLC is

$$\varepsilon_{\text{rslc}} = \sqrt{\frac{\int_A [S_g(\theta, \varphi, t_0) - S_n(\theta, \varphi, t_0)]^2 dA}{\int_A [S_g(\theta, \varphi, t_0)]^2 dA}}, \quad (29)$$

where $S_g(\theta, \varphi, t_0)$ and $S_n(\theta, \varphi, t_0)$ are the solutions from the Green's function and finite-element methods, respectively, and the integration is over the entire surface.

The RSLC, vertical rate and vertical displacement predicted from both the finite-element models and the Green's function methods show that the present-day RSLC is $\sim 10 \text{ mm yr}^{-1}$ (in our notation, a positive RSLC is for a falling sea level, which makes the comparison with vertical rates easier) for North America and Fennoscandia and $\sim 20 \text{ mm yr}^{-1}$ for the Antarctic (Fig. 4a). The predicted present-day vertical displacement for North America and Antarctica are ~ 50 and 100 m , respectively (Fig. 4b). Finite-element solutions generally agree with the Green's function solutions (Table 3). For case B1 with

a horizontal resolution of $\sim 135 \text{ km}$, a vertical resolution of $\sim 70 \text{ km}$ (the grid is refined in the upper mantle and lithosphere), and Δt of 200 and 100 yr for the glaciation (i.e. the first 90 ka) and post-glaciation periods, respectively, the numerical errors are $\sim 5\text{--}6$ per cent for present-day RSLC, vertical rate and displacement, and are slightly smaller (~ 3 per cent) for 10 and 28 ka ago (Table 3). Note that 28 ka ago is in the glaciation period where we assumed a simple linear loading time function and that the errors tend to be smaller during this period.

Case B2 uses the same spatial resolution but a doubled temporal resolution, compared with case B1 (Table 3). The errors remain about the same in the glaciation period (i.e. at $t = -28 \text{ ka}$) but are reduced in the post-glaciation period (at $t = -10$ and 0 ka) (Table 3). This suggests that increasing temporal resolution is only important for the post-glacial period during which the rather rapid changes in ice distribution in the ICE-3G require high temporal resolution. Case B3 with the same temporal resolution but higher spatial resolution in comparison with case B1 shows that spatial resolution is important for reducing the errors during the glaciation period (Table 3). The errors for the vertical rate and the displacement at $t = -28 \text{ ka}$ are reduced to ~ 0.6 per cent for case B3 from

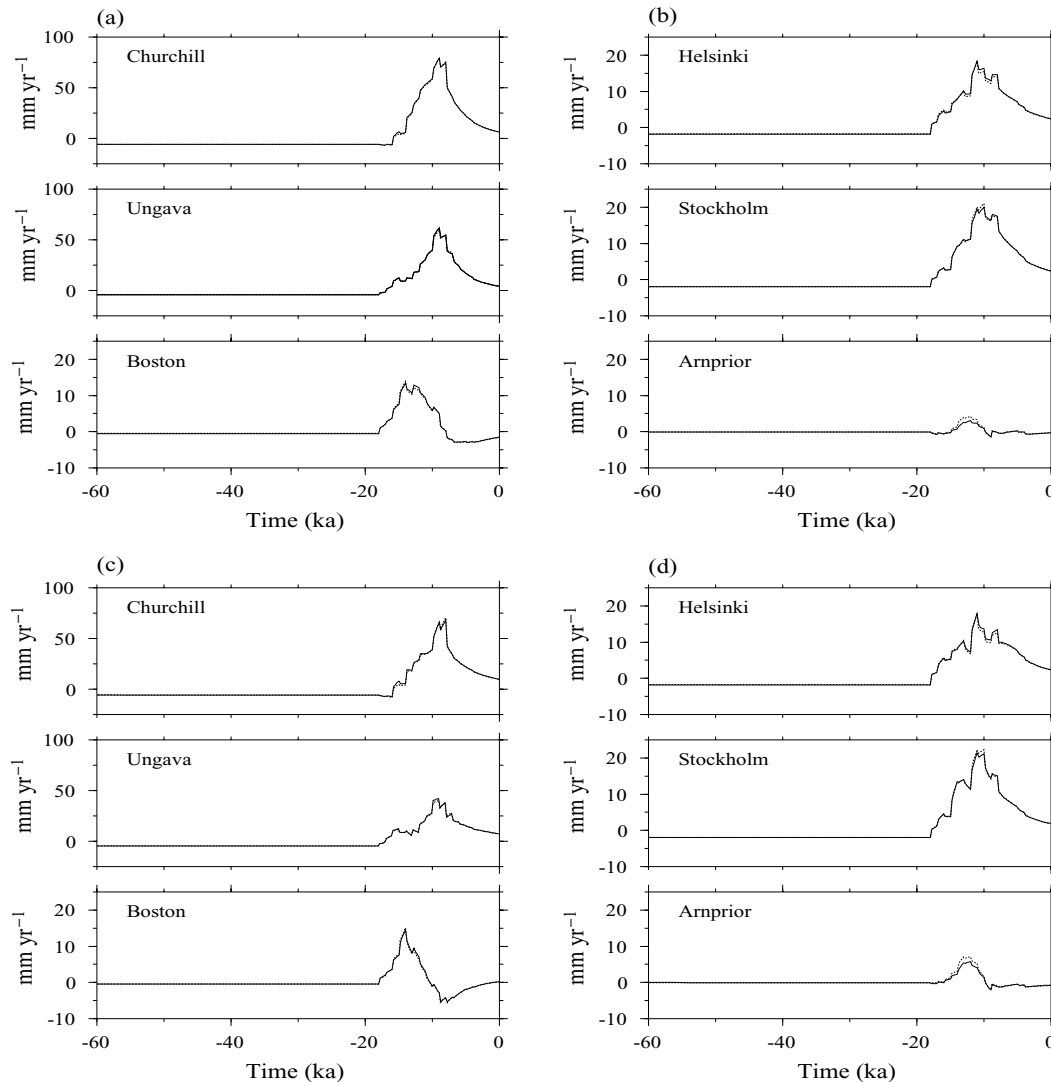


Figure 6. Time-dependent RSLC from the finite-element method (solid lines) and semi-analytic solutions (dashed lines) for the last 60 ka at six different sites for cases B4 (a and b) and B5 (c and d). The coordinates for Churchill, Ungava, Boston, Helsinki, Stockholm and Arnprior are ($N59^\circ, 266^\circ$), ($N60^\circ, 285^\circ$), ($N42^\circ, 289^\circ$), ($N60^\circ, 25^\circ$), ($N59^\circ, 18^\circ$) and ($N56^\circ, 356^\circ$), respectively.

~2.3 per cent in case B1 (Table 3). For case B3, the error for RSLC at $t = -28$ ka is about twice of that for the vertical rate (Table 3). This arises mainly because we only use the first 20 spherical harmonics in the calculation of the gravitational potential. When there is still ice present (i.e. until 5 ka ago in ICE-3G), the contribution to the RSLC from the relatively short-wavelength ($>$ degree 20) potential of the ice distribution may not be accurately described in our finite-element calculation. Although this effect exists for all the cases in Table 3, our numerical experiments show that the predicted RSLC is sufficiently accurate. For case B3, the errors for $t = 0$ and -10 ka are also reduced compared with case B1, but not as dramatically as for $t = -28$ ka.

In case B4, time increments are 200 and 25 yr for the glaciation and post-glaciation periods, respectively, and the spatial resolution is the same as in case B3 (Table 3). Now we also observe significant reduction of errors for the post-glaciation period (e.g. the present-day RSLC error is 1.49 per cent) (Table 3). However, the error for the present-day total displacement is still ~3.4 per cent (Table 3). In Fig. 5, we present the RSLC, vertical rate and displacement for the present day and 10 ka ago along two profiles (270° longitude passing through North America and Antarctica and 55° northern latitude passing through North America). In Figs 6(a) and (b) we show the time-dependent RSLC in the last 60 ka for six different sites in North

America (Churchill, Ungava and Boston) and Fennoscandia and its surrounding region (Helsinki, Stockholm and Arnprior of Scotland) from both finite-element (solid lines in these figures) and Green's function (dashed lines) methods (coordinates for these sites are given in the caption for Fig. 6). Our finite-element method reproduces the Green's function solutions almost exactly except for Arnprior of Scotland where the finite-element method underestimates the RSLC around $t = -12$ ka (Fig. 6b).

We have also computed a case with a much weaker upper mantle (case B5 with 3×10^{20} and 10^{22} Pa s viscosity for the upper mantle and lower mantle, respectively). The difference in mantle viscosity is the only difference between cases B5 and B4. The errors for this case with larger variations in mantle viscosity are similarly small (Table 3 and Figs 6c and d). That the errors for cases B4 and B5 are small indicates that we can use our finite-element model to examine the effects of laterally varying structures, including the variable lithospheric thickness considered in the next section.

5 EFFECTS OF VARIABLE LITHOSPHERIC THICKNESS

We now apply our finite-element model to study the effects of laterally varying structure on the PGR. The focus in this paper is

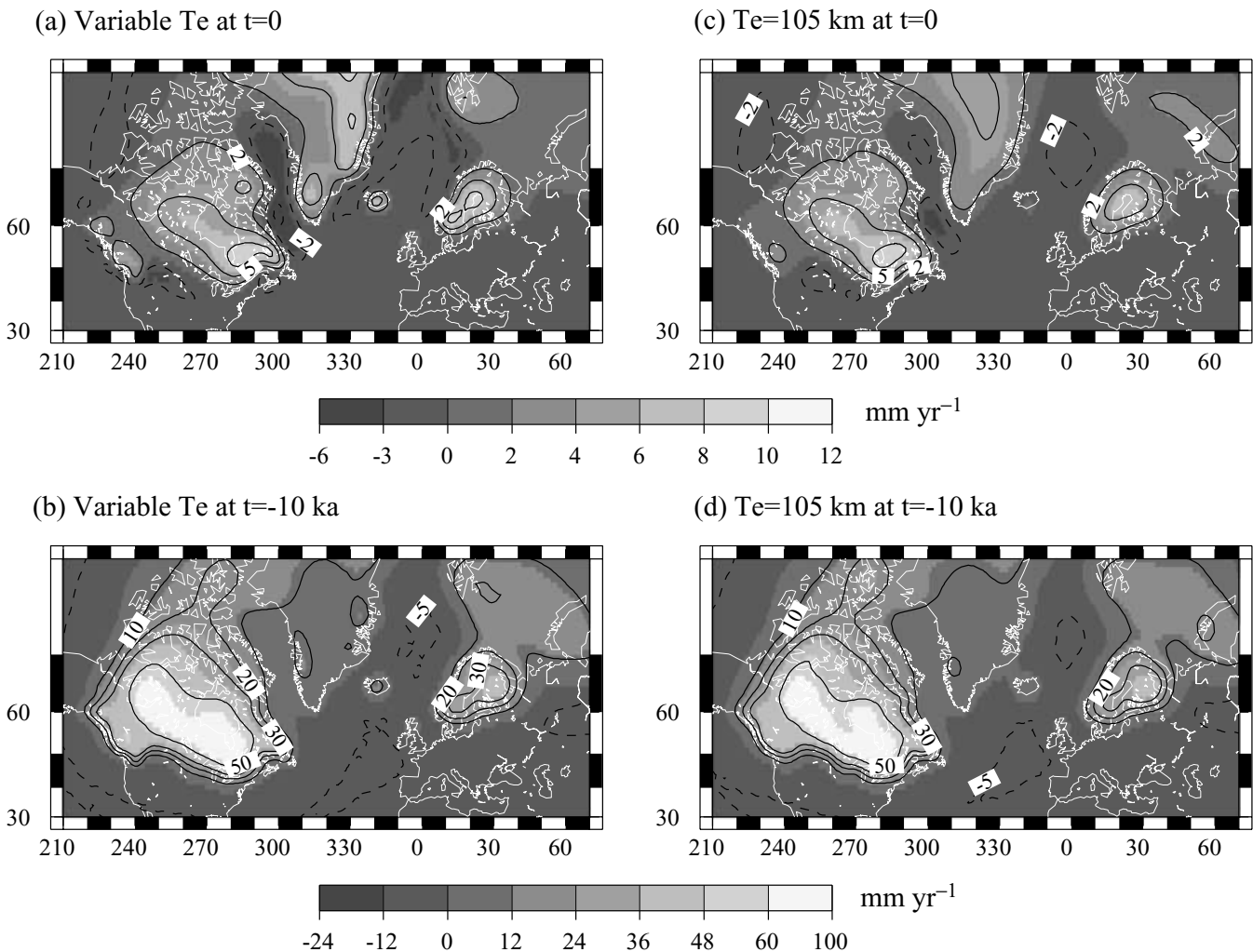


Figure 7. RSLC for North America and Fennoscandia from case C1 with variable lithospheric thickness at $t = 0$ (a) and $t = -10$ ka (b) and a case with uniform 105 km thick lithosphere at $t = 0$ (c) and $t = -10$ ka (d). Dashed contours are for negative values.

on the effects of variable lithospheric thickness (Fig. 1), while the influence of laterally varying mantle viscosity will be discussed in future papers. Our goal is to examine to what extent the response of an Earth with a lithosphere of laterally varying thickness can be modelled by assuming a lithosphere of constant thickness.

5.1 Distribution of lithospheric thickness

The lithospheric thickness in Fig. 1 is derived from a compilation of elastic plate thicknesses from Watts (2001). For oceanic regions, the elastic thickness as constrained from observed topography and gravity at seamounts is controlled by the $\sim 500^\circ\text{C}$ geotherm (Watts *et al.* 1980). Since younger seafloor leads to shallower depth for 500°C , younger seafloor tends to have smaller elastic thickness. However, a more reasonable mechanical model for the oceanic mantle employs a viscoelastic rheology that indicates that on a timescale of ~ 100 ka the apparent elastic thickness should be significantly larger than that derived from the long-term seamount loads (e.g. Watts & Zhong 2000). For this reason, we use the 750°C geotherm to define the oceanic lithospheric thickness for our PGR calculations. With lithospheric thermal structure determined from a half-space cooling for a given seafloor age, the oceanic lithospheric thickness may vary from a few kilometres at spreading centres to ~ 80 km at old ocean basins (e.g. in the western Pacific).

Lithospheric thickness variations on continents are more complicated because of their complicated tectonic history. In general, old continental cratons and shields have considerably larger elastic thickness (e.g. > 100 km for the eastern US and Canadian shields) than young tectonically active areas (e.g. ~ 10 km for the western

US), as constrained by studies of long-term loads (e.g. Bechtel *et al.* 1990; Zuber *et al.* 1989; Simons *et al.* 2000). The distribution of continental elastic thickness is generally consistent with observations of heat flux (Jaupart *et al.* 1998) and the upper-mantle seismic structure (e.g. Grand 1994; Ritzwoller & Lavelly 1995; van der Lee & Nolet 1997). For our PGR studies, to consider possible relaxation effects we take the continental lithospheric thickness to be 1.6 times that of the elastic thickness estimated from loading studies and from heat flux observations. Admittedly, there are some uncertainties with our lithospheric thickness model in Fig. 1, particularly for continental regions. However, we think that its general pattern is robust.

There are significant lateral variations in lithospheric thickness in the regions surrounding the locations of the major ice sheets including in North America and Fennoscandia. The North American ice sheets existed in a region where the lithospheric thickness is as large as 200 km, but the surrounding regions, including the western US and the northwest Atlantic Ocean, have a much thinner lithosphere (Fig. 1). The Fennoscandian ice sheets were located where there is a significant increase in lithospheric thickness toward the east (Fig. 1). We have computed averaged lithospheric thickness in these formerly glaciated regions. The averaging is done over regions with different radii from the centres of the ice sheets. For North America, the averaged lithospheric thicknesses over 15° , 30° and 45° radii from the Hudson Bay with latitude $N59^\circ$ and longitude $E271^\circ$ are 140, 105 and 83 km, respectively. For Fennoscandia, the averaged lithospheric thicknesses over 9.5° , 19° and 28.5° radii from latitude $N63^\circ$ and longitude $E21.5^\circ$ are 70, 73 and 74 km, respectively. For comparison, the globally averaged lithospheric thickness is 56 km.

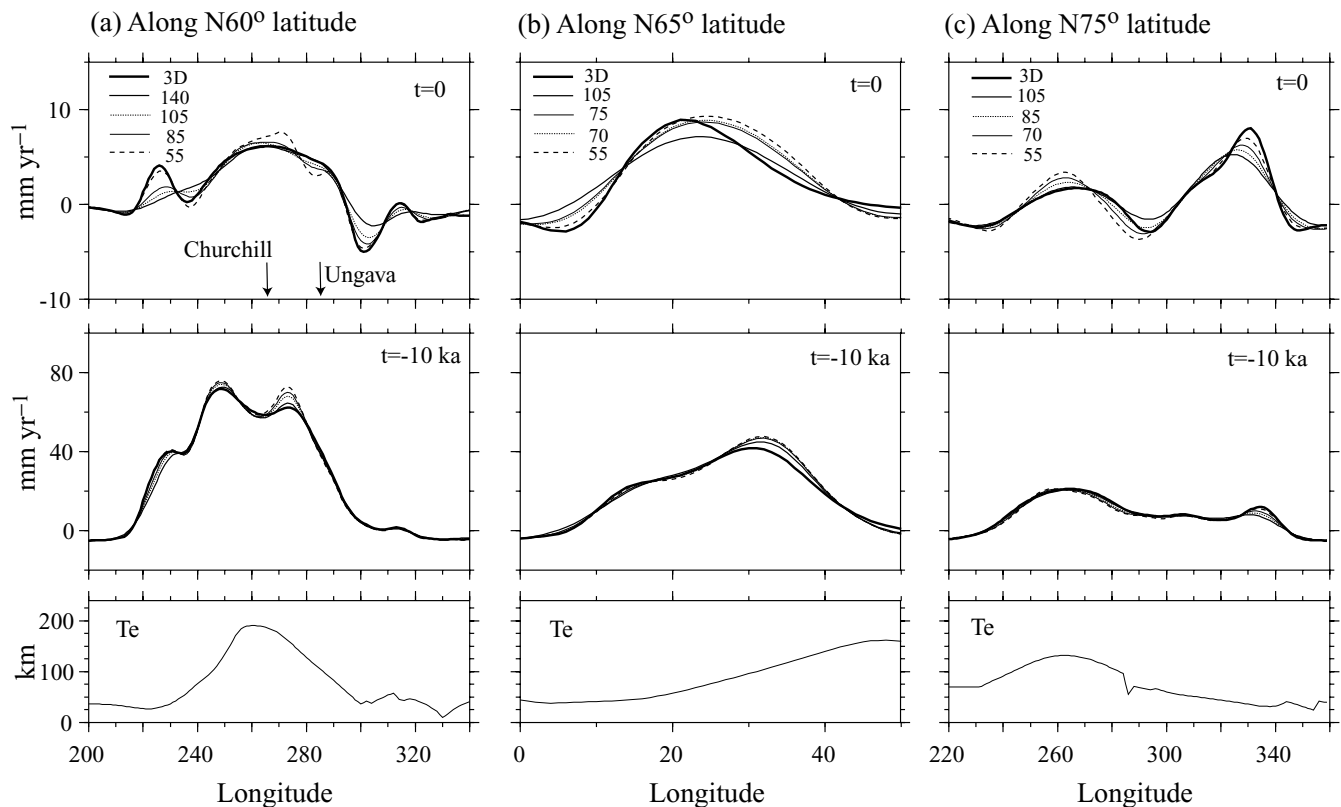


Figure 8. RSLC from case C1 and cases with uniform lithospheric thicknesses along profiles $N60^\circ$ latitude for North America (a), $N65^\circ$ latitude for Fennoscandia (b), and $N75^\circ$ latitude for Greenland (c). For 8(a)–(c), the top and middle panels are RSLC at $t = 0$ and -10 ka, respectively, and the bottom panel shows the lithospheric thickness variations from Fig. 1. The thicknesses for cases with uniform lithospheric thickness are labelled in the middle panel. Churchill and Ungava are also marked since their latitudes are $\sim N60^\circ$.

5.2 Calculations with variable lithospheric thickness

We now examine the effects of laterally varying lithospheric thickness on the PGR observations of RSLC. We first present case C1 that includes the lithospheric structure in Fig. 1 and the same viscosity structure as in case B4 (i.e. viscosities in the upper mantle and lower mantle are 10^{21} and 2×10^{21} Pa s, respectively; see Table 3). Case C1 uses the same spatial and temporal resolutions as those in case B4 that have been demonstrated to adequately resolve the solutions in the spherically symmetric case. For comparison, we also compute results for spherically symmetric cases that have the same mantle viscosity profiles as case B4, but have different uniform lithospheric thicknesses ranging from 45 to 200 km.

Fig. 7 shows the predicted RSLC for North America and Fennoscandia at $t = 0$ and -10 ka for case C1, and for a case with a uniform 105 km thick lithosphere. The RSLC at $t = -10$ ka from these two cases is broadly similar (Figs 7b and d), but for the present-day RSLC case C1 generally predicts larger spatial variability (Figs 7a and c). More specifically, case C1 predicts larger rates of present-day sea level rise in Davis Strait, Baffin Bay, the Atlantic coasts north of $N60^\circ$, and western Canada, and larger rates

of sea level fall in Fennoscandia and Greenland, than the case with a uniform 105 km thick lithosphere. Since 105 km is the averaged thickness within 15° (~ 1670 km) of the centre of Hudson Bay (see Section 5.1), this uniform lithospheric thickness case may be relevant only for North America. It is therefore important to examine predictions from cases with other uniform lithospheric thicknesses.

The RSLC for $t = 0$ and -10 ka from case C1 and cases with different uniform lithospheric thicknesses along profiles $N60^\circ$ for North America, $N65^\circ$ for Fennoscandia and $N75^\circ$ for Greenland show that the RSLC may be sensitive only to the local lithospheric thickness (Fig. 8). At $t = -10$ ka, while models with different lithospheric structure produce rather similar RSLC (middle panels in Fig. 8), noticeable differences occur among these models at 275° longitude on the North American profile and 32° longitude on the Fennoscandian profile. At these locations, lithospheric thicknesses are greater than 100 km (bottom panels in Fig. 8), and the uniform thickness cases with small lithospheric thickness show larger deviations from case C1 than do cases where the uniform lithospheric thickness is similar to the large values at those locations in case C1.

That the local lithospheric thickness has significant controls on RSLC can be seen more clearly from the present-day RSLC, where

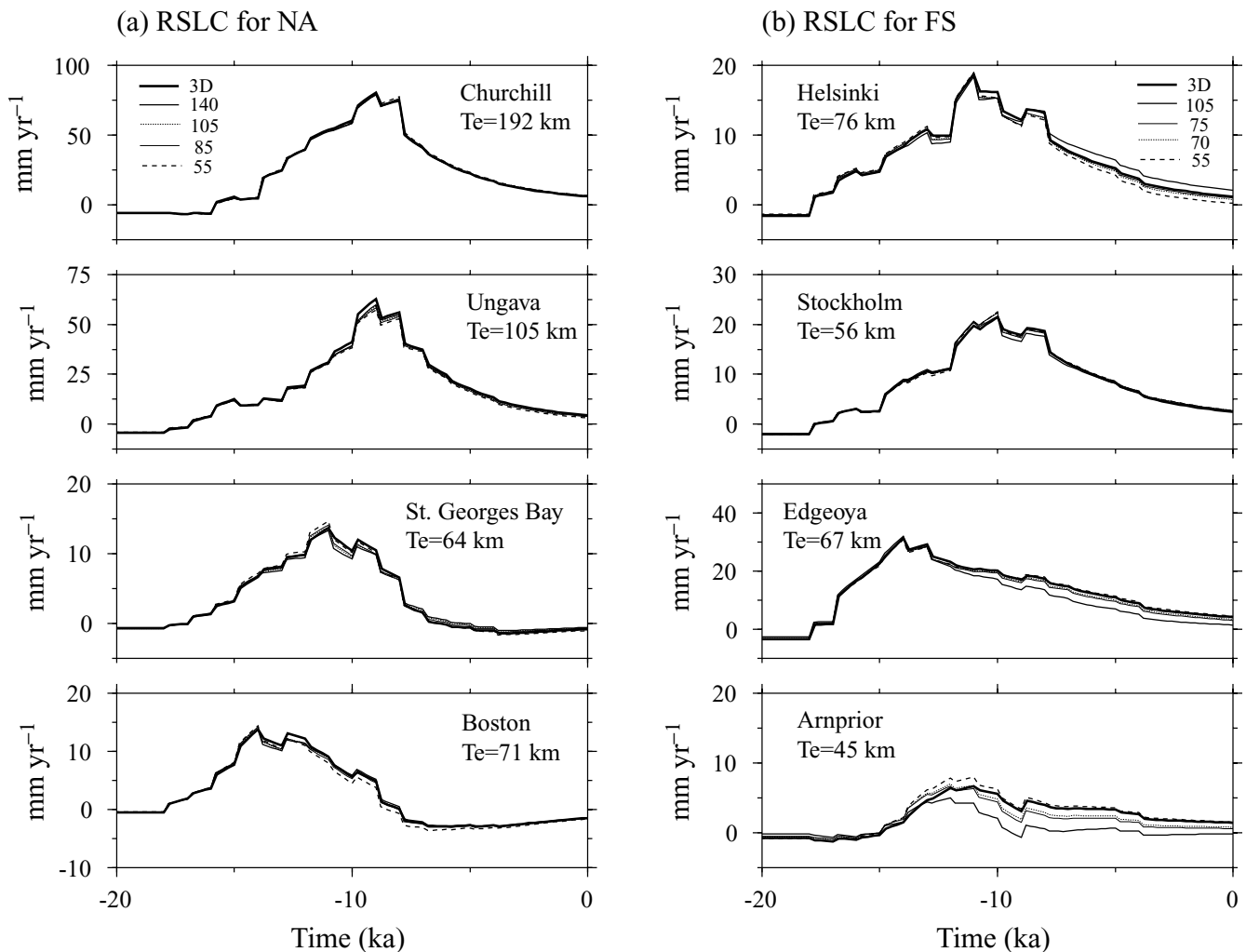


Figure 9. Time-dependent RSLC during the last 20 ka at Churchill, Ungava, St Georges Bay and Boston in North America (a), and at Helsinki, Stockholm, Edgeoya, and Arnprior of Scotland in Europe (b), from case C1 and cases with uniform lithospheric thicknesses. The lithospheric thickness is also marked for each site. The coordinates for St Georges Bay and Edgeoya are ($N48.5^\circ$, 301.5°) and ($N78^\circ$, 23°), respectively. The coordinates for other sites are given in Fig. 6.

the differences between different models are relatively large (top panels in Fig. 8). For example, in the North American profile (Fig. 8a), while all the uniform lithospheric thickness cases except the 55 km case reproduce the results from case C1 well at the centre of the formerly glaciated region (at $\sim 270^\circ$ longitude), cases with large uniform lithospheric thickness (e.g. 140 and 105 km) fail to reproduce case C1 on either side of the ice centre at 300° longitude (i.e. Davis Strait) and 225° longitude (i.e. western Canada). However, in Davis Strait and western Canada, the results obtained assuming relatively small uniform lithospheric thicknesses (e.g. 55 km) agree well with case C1. In Davis Strait and western Canada lithospheric thicknesses are ~ 50 km, significantly smaller than that at the ice centre (Fig. 1 and bottom panel of Fig. 8a). The relatively thin lithosphere allows deformation at short wavelengths that may be impossible for thicker lithospheres. For the Fennoscandian profile, the lithosphere thickens from west to east, and cases with thick (thin) lithosphere (e.g. 105 km) agree with case C1 well on the eastern (western) portion of the profile (Fig. 8b). Similar results can be seen for the Greenland profile (Fig. 8c).

To examine the full time dependence, we compute the RSLC history at eight different sites in North America (Churchill, Ungava,

St Georges Bay and Boston) and Fennoscandia and its surrounding regions (Helsinki, Stockholm, Edgeoya and Arnprior). For the four North American sites, the RSLC does not show a significant dependence on the lithospheric thickness (Fig. 9a). However, different lithospheric structure results in a significant difference at Helsinki, Edgeoya and Arnprior (Fig. 9b). For these three sites, case C1 with laterally varying lithospheric thickness is best reproduced by uniform lithospheric thickness cases in which the thickness is similar to the local lithospheric thickness in case C1. For example, at Helsinki where the lithospheric thickness is 76 km according to Fig. 1, the RSLC from case C1 is well reproduced by the case with uniform lithospheric thickness of 75 km. Models with a thinner (thicker) lithosphere may underestimate (overestimate) the RSLC.

To further examine the dependence of the RSLC on lithospheric thickness, we compute the relative difference in the RSLC over the last 20 ka at those eight different sites between case C1 and cases with uniform lithospheric thickness ranging from 45 to 200 km. The relative differences at Churchill and Ungava are < 10 per cent for all the lithospheric thicknesses (Fig. 10a). However, at Arnprior, Edgeoya and Helsinki, the relative differences show larger variations with the lithospheric thickness (Fig. 10a). This indicates that

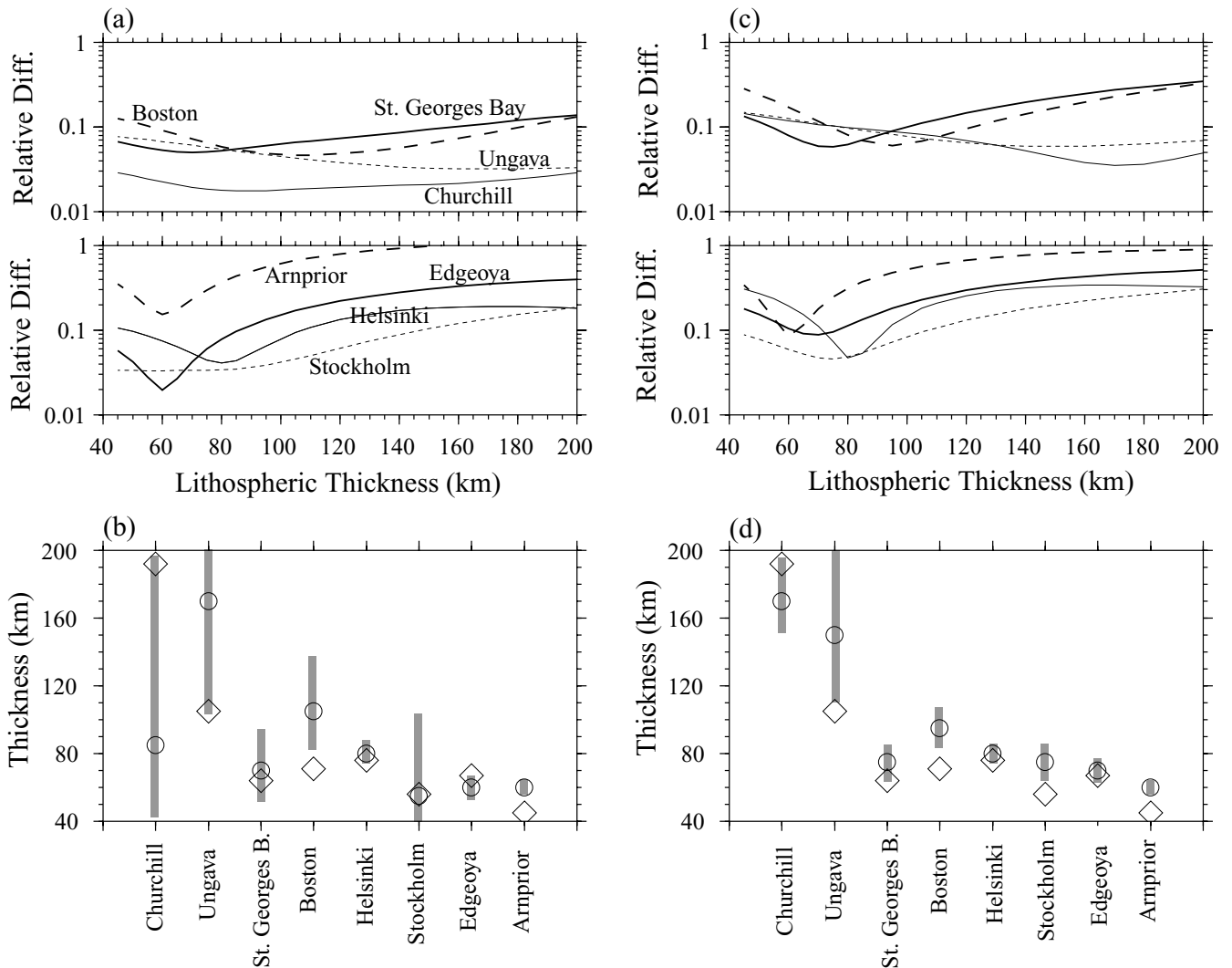


Figure 10. Relative difference of the RSLC at eight different sites over the last 20 ka, between case C1 and cases with different uniform lithospheric thicknesses (a), and the optimal (circles) and actual (diamonds) lithospheric thickness at each site (b). The shaded bar in (b) indicates the range of lithospheric thicknesses that leads to relative differences within 1 per cent of the minimum relative difference. Parts (c) and (d) are the same as (a) and (b) but for case C2.

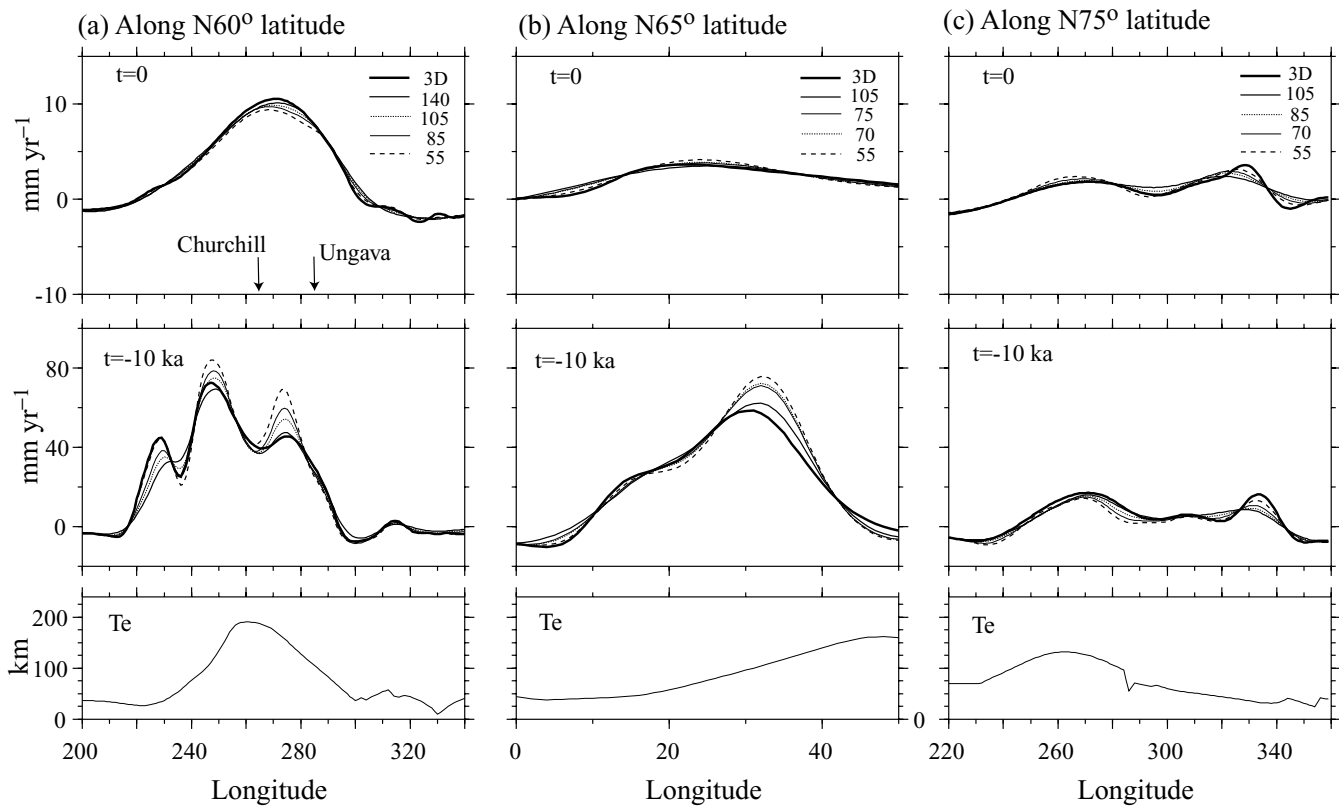


Figure 11. Same as Fig. 8 but for case C2, and for uniform lithospheric thickness cases where the mantle viscosity is same as that in case C2.

the RSLC shows different sensitivity to the lithospheric thickness, depending on the sites. In general, sites at the centre of a large ice sheet (e.g. North American) are less sensitive to the lithospheric thickness than sites at the periphery bulge or near a small ice sheet.

We may determine an optimal lithospheric thickness at each site from the minimum relative difference. Fig. 10(b) shows these optimal thicknesses (circles) along with the actual lithospheric thicknesses (diamonds) at each site. The optimal and actual lithospheric thicknesses are generally similar except at Churchill, Ungava and Boston (Fig. 10b). Since the RSLC at some sites is relatively insensitive to lithospheric thickness, a large range of lithospheric thickness may lead to similarly small relative differences (e.g. for Churchill in Fig. 10a). For this reason, we also show in Fig. 10(b) the range of lithospheric thickness (shaded bars) that yields relative differences within 1 per cent of the minimum relative differences. At Churchill and Ungava the actual lithospheric thickness falls in this range, but at Boston and Arnprior the actual lithospheric thickness is outside of this range by ~ 10 km (Fig. 10b). These anomalies at Boston and Arnprior may be related to the fact that these two sites are both close to the peripheral bulges of the rebound patterns. However, we also recognize that these anomalies may be related to our rather arbitrary choice of designating 1 per cent of the minimum relative difference to determine the range of lithospheric thickness. In general, though, these results do tend to confirm the influence of local lithospheric thickness on the RSLC.

We now present results for a case (case C2) that differs from case C1 only in the viscosity structure of the mantle (3×10^{20} and 10^{22} Pa s for the upper and lower mantle, respectively). For this viscosity structure, we also compute cases with different uniform lithospheric thicknesses, to compare with the variable thickness case. Now the differences in the predicted RSLC among cases with dif-

ferent lithospheric structure are much more significant at $t = -10$ ka than that for the present day (Fig. 11). In general, when a significant difference occurs at a certain location among different cases, it is always the uniform lithospheric thickness case where the thickness is similar to the local lithospheric thickness that best reproduces the RSLC from case C2. This is consistent with the results from the case C1 viscosity profile (e.g. Fig. 8). For example, for the North American profile at $t = -10$ ka, significant differences can be seen at longitudes 228° , 248° and 275° (Fig. 11a). At longitude 228° , the lithospheric thickness is < 50 km and the case with a uniform lithospheric thickness of 55 km best reproduces case C2. At longitudes 248° and 275° where lithospheric thicknesses are ~ 100 km or larger, the cases with 105 and 140 km uniform lithospheric thickness reproduce case C2 well. Similar trends can be seen along the Fennoscandian and Greenland profiles (Figs 11b and c).

The time-dependent RSLC at individual sites from case C2 and other uniform lithospheric thickness cases confirms the effects of local lithospheric thickness. At Churchill and Ungava, the RSLC is not very sensitive to lithospheric structure. At St Georges Bay and Boston, significant differences occur around $t = -10$ ka among the different cases. However, cases with uniform lithospheric thickness that are similar to the local thickness reproduce case C2 well (Fig. 12a). For Helsinki, Edgeoya and Arnprior, the RSLC is very sensitive to the lithospheric thickness around $t = -10$ ka. Again, the local lithospheric thickness controls the RSLC (Fig. 12b). We have also computed the relative difference in the RSLC at these eight sites between case C2 and various uniform lithospheric thickness cases (Fig. 10c). At each site, the actual lithospheric thickness falls within or close to the range of lithospheric thicknesses (Fig. 10d) where there is a good agreement between the uniform thickness models and case C2.

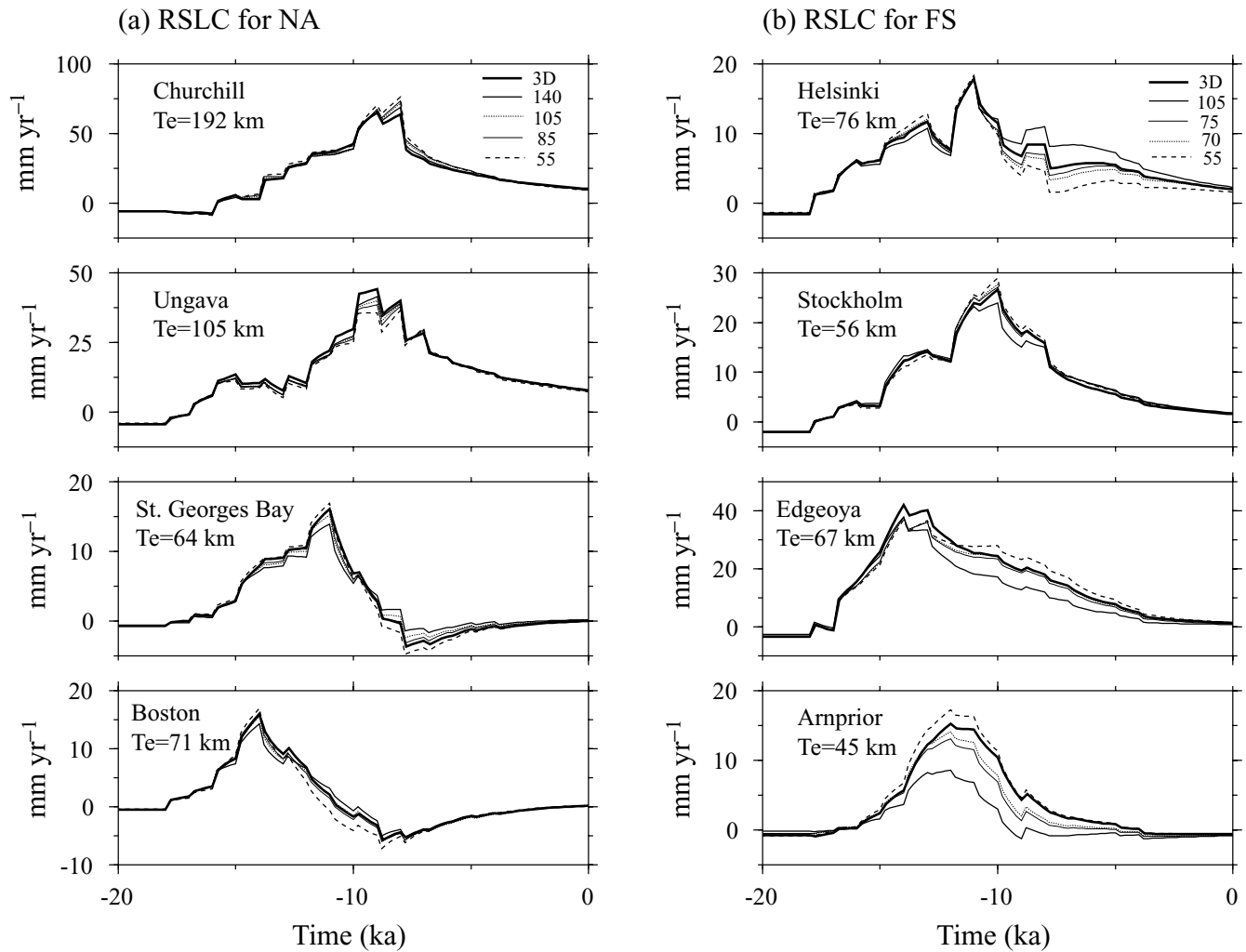


Figure 12. Same as Fig. 9 but for case C2, and for uniform lithospheric thickness cases where the mantle viscosity is same as that in case C2.

6 CONCLUSIONS AND DISCUSSIONS

We have developed a 3-D spherical finite-element model for the Earth's viscoelastic deformation in response to surface loads. Our model includes self-gravitation effects. The mantle in our model is assumed to be incompressible but it can have a fully 3-D viscosity structure. Benchmarks against Green's function solutions for loading problems with 1-D mantle structure demonstrate the accuracy of our finite-element model in predicting the time-dependent surface deformation rate, displacement and relative sea level changes (RSLC). Coupled with efficient parallel computing, we believe that the finite-element model that we present here can be used to address a variety of viscoelastic deformation in geodynamics.

We have applied our finite-element model, forced with the ICE-3G deglaciation model of Tushingham & Peltier (1991), to study the effects of laterally varying lithospheric thickness on observations (e.g. surface deformation rates and RSLC) of post-glacial rebound. The laterally varying lithospheric thicknesses are derived from estimates of the thermal structure of oceanic lithosphere and from elastic thicknesses on continents as estimated from studies of long-term geological loads (e.g. mountains and sediments) (Watts 2001). Our calculations show that the effects of lithospheric structure on the RSLC depend on the locations of the observation sites and on the

size of ice sheets. The RSLC near the centre of the North American ice sheet is much less sensitive to lithospheric thickness than the RSLC at the centre of the Fennoscandian ice sheet, consistent with a previous suggestion (e.g. Tushingham & Peltier 1991). Outside the loads and at the peripheral bulges the RSLC tends to be more sensitive to lithospheric thickness. Our results show that the RSLC is mainly controlled by local lithospheric thickness. The RSLC at a given location, as predicted using models with laterally varying lithospheric thickness, can be reproduced using a 1-D model with a uniform lithospheric thickness equal to the local lithospheric thickness. This conclusion is generally consistent with that from 2-D model calculations by Kaufmann *et al.* (1997).

Our results have implications for PGR studies, especially for those on a global scale. Because models with 3-D structures are computationally significantly more expensive than those with 1-D structures, our results may provide useful guidance in improving the 1-D models. As we have demonstrated, for a given 1-D mantle viscosity structure and ice model the RSLC predicted for an Earth with laterally varying lithospheric thickness can be best modelled using the lithospheric thickness at each local site. PGR studies often use a single lithospheric thickness that best characterizes formerly glaciated regions to model the RSLC or other PGR observations at any location, in both regional (e.g. Nakada & Lambeck 1989) and global models

(e.g. Peltier 1998). Our results indicate that although this approach should work well for the RSLC near the centre of formerly glaciated regions, it may not be adequate outside of formerly glaciated regions if these regions have a significantly different lithospheric thickness from that at the centres of ice sheets as they often do (e.g. along the edges of the North American continent). Our results suggest that it is more appropriate to compute uniform lithospheric thickness models with a range of lithospheric thicknesses and to use the PGR signals predicted from the model with a thickness that is similar to that at each observation site. For ice sheets with a large horizontal extent (e.g. in North America), because the PGR signals near the centres of ice sheets are relatively insensitive to lithospheric thickness, we may use the characteristic lithospheric thickness for observational sites outside the ice sheets, instead of that for the formerly glaciated regions, in models with 1-D structures.

We believe that this study represents an important step towards understanding the effects of laterally varying structure on the PGR signals. With parallel computing technology and advanced numerical techniques, the computational tools that we present here enable us to simulate the PGR signals at high resolutions for an Earth with 3-D structures in response to realistic ice models. In future studies, we will focus on the effects of laterally varying viscosity on the PGR signals, and we will also include the compressibility.

ACKNOWLEDGMENTS

This research is supported by NSF Grant EAR-0087567. We thank P. Wu for a helpful review and A. B. Watts for the global elastic thickness data set. NPACI provides some computational support for this work.

REFERENCES

- Bechtel, T.D., Forsyth, D.W., Sharpston, V.L. & Grieve, R.A., 1990. Variations in effective elastic thickness of the north American lithosphere, *Nature*, **343**, 636–638.
- Cathles, L.M., 1975. *The Viscosity of the Earth's Mantle*, p. 390, Princeton, Princeton University Press.
- Forte, A.M. & Mitrovica, J.X., 1996. New inferences of mantle viscosity from joint inversion of long-wavelength mantle convection and post-glacial rebound data, *Geophys. Res. Lett.*, **23**, 1147–1150.
- Gasparini, P. & Sabadini, R., 1989. Lateral heterogeneities in mantle viscosity and post-glacial rebound, *Geophys. J. Int.*, **98**, 413–428.
- Giunchi, C., Spada, G. & Sabadini, R., 1997. Lateral viscosity variations and post-glacial rebound: effects on present-day VLBI baseline deformations, *Geophys. Res. Lett.*, **24**, 13–16.
- Grand, S.P., 1994. Mantle shear structure beneath the Americas and surrounding oceans, *J. geophys. Res.*, **99**, 11 591–11 622.
- Hager, B.H. & Richards, M.A., 1989. Long-wavelength variations in Earth's geoid: physical models and dynamical implications, *Phil. Trans. R. Soc. Lond., A*, **328**, 309–327.
- Han, D. & Wahr, J., 1995. The viscoelastic relaxation of a realistically stratified earth and a further analysis of post-glacial rebound, *Geophys. J. Int.*, **120**, 287–311.
- Hughes, T.J.R., 1987. *The Finite Element Method: Linear Static and Dynamic Finite Element Analysis*, Prentice-Hall, Englewood Cliffs.
- Jaupart, C., Mareschal, J.-C., Guillou-Frottier, L., Davaille, A., 1998. Heat flow and thickness of the lithosphere in the Canadian Shield, *J. geophys. Res.*, **103**, 15 269–15 286.
- Kaufmann, G. & Wolf, D., 1999. Effects of lateral viscosity variations on postglacial rebound: an analytical approach, *Geophys. J. Int.*, **137**, 489–500.
- Kaufmann, G. & Wu, P., 1998. Lateral asthenospheric viscosity variations and postglacial rebound: a case study for the Barents Sea, *Geophys. Res. Lett.*, **25**, 1963–1966.
- Kaufmann, G. & Wu, P., 2002. Glacial isostatic adjustment in Fennoscandia with a three-dimensional viscosity structure as an inverse problem, *Earth planet. Sci. Lett.*, **197**, 1–10.
- Kaufmann, G., Wu, P. & Wolf, D., 1997. Some effects of lateral heterogeneities in the upper mantle on postglacial land uplift close to continental margins, *Geophys. J. Int.*, **127**, 175–187.
- Kaufmann, G., Wu, P. & Li, G., 2000. Glacial isostatic adjustment in Fennoscandia for a laterally heterogeneous Earth, *Geophys. J. Int.*, **143**, 262–273.
- Lambeck, K., Johnson, P. & Nakada, M., 1990. Holocene glacial rebound and sea level change in NW Europe, *Geophys. J. Int.*, **103**, 451–468.
- Martinec, Z., 1999. Spectral, initial value approach for viscoelastic relaxation of a spherical earth with a three-dimensional viscosity—I. Theory, *Geophys. J. Int.*, **137**, 469–488.
- Martinec, Z., 2000. Spectral-finite element approach to three-dimensional viscoelastic relaxation in a spherical earth, *Geophys. J. Int.*, **142**, 117–141.
- Martinec, Z., Cadek, O. & Fleitout, L., 2001. Can the 1D viscosity profiles inferred from postglacial rebound be affected by lateral viscosity variations in the tectosphere?, *Geophys. Res. Lett.*, **28**, 4403–4406.
- Mitrovica, J.X. & Forte, A.M., 1997. Radial profile of mantle viscosity: results from the joint inversion of convection and postglacial rebound observables, *J. geophys. Res.*, **102**, 2751–2769.
- Mitrovica, J.X. & Peltier, W.R., 1991. A complete formation for the inversion of post-glacial rebound data: resolving power analysis, *Geophys. J. Int.*, **104**, 267–288.
- Moresi, L. & Gurnis, M., 1996. Constraints on the lateral strength of slabs from three-dimensional dynamic flow models, *Earth planet. Sci. Lett.*, **138**, 15–28.
- Moresi, L. & Solomatov, V.S., 1995. Numerical investigation of 2-D convection with extremely large viscosity variations, *Phys. Fluids*, **7**, 2154–2162.
- Nakada, M. & Lambeck, K., 1989. Late Pleistocene and Holocene sea-level change in the Australian region and mantle rheology, *Geophys. J.*, **96**, 497–517.
- Ni, Z. & Wu, P., 1998. Effects of removing concentric positioning on post-glacial vertical displacements in the presence of lateral variation in lithospheric thickness, *Geophys. Res. Lett.*, **25**, 3209–3212.
- Peltier, W.R., 1976. Glacial-isostatic adjustment II. The inverse problem, *Geophys. J. R. astr. Soc.*, **46**, 669–705.
- Peltier, W.R., 1998. Postglacial variations in the level of the sea: Implications for climate dynamics and solid-Earth geophysics, *Rev. Geophys.*, **36**, 603–689.
- Ritzwoller, M.H. & Lavelle, E.M., 1995. Three-dimensional seismic models of the Earth's mantle, *Rev. Geophys.*, **33**, 1–66.
- Sabadini, R., Yuen, D.A. & Portney, M., 1986. The effects of upper mantle lateral heterogeneities on postglacial rebound, *Geophys. Res. Lett.*, **13**, 337–340.
- Simons, M. & Hager, B.H., 1997. Localization of the gravity field and the signature of glacial rebound, *Nature*, **390**, 500–504.
- Simons, F.J., Zuber, M.T. & Korenaga, J., 2000. Isostatic response of the Australian lithosphere: estimation of effective elastic thickness and anisotropy using multitaper spectral analysis, *J. geophys. Res.*, **105**, 19 163–19 184.
- Tromp, J. & Mitrovica, J.X., 1999. Surface loading of a viscoelastic planet II. Spherical models, *Geophys. J. Int.*, **137**, 856–872.
- Tromp, J. & Mitrovica, J.X., 2000. Surface loading of a viscoelastic planet III. Aspherical models, *Geophys. J. Int.*, **140**, 425–441.
- Tushingham, A.M. & Peltier, W.R., 1991. ICE-3G: a new global model of Late Pleistocene deglaciation based upon geophysical predictions of post-glacial relative sea level change, *J. geophys. Res.*, **96**, 4497–4523.
- Van der Lee, S. & Nolet, G., 1997. Upper mantle *S* velocity structure of North America, *J. geophys. Res.*, **102**, 22 815–22 838.
- Wahr, J., vanDam, T., Larson, K. & Francis, O., 2001. Geodetic measurements in Greenland and their implications, *J. geophys. Res.*, **106**, 16 567–16 582.
- Watts, A.B., 2001. *Isostasy and Flexure of the Lithosphere*, Cambridge University Press, Cambridge.
- Watts, A.B. & Zhong, S., 2000. Observations of flexure and the rheology of oceanic lithosphere, *Geophys. J. Int.*, **142**, 855–875.

- Watts, A.B., Bodine, J.H. & Ribe, N.M., 1980. Observations of flexure and the geological evolution of the Pacific ocean basin, *Nature*, **283**, 532–537.
- Wu, P., 1992. Deformation of an incompressible viscoelastic flat earth with power-law creep: a finite element approach, *Geophys. J. Int.*, **108**, 136–142.
- Wu, P., 1993. Postglacial rebound in a power-law medium with axial symmetry and the existence of the transition zone in relative sea-level data, *Geophys. J. Int.*, **114**, 417–432.
- Wu, P., 1995. Can observations of postglacial rebound tell whether the rheology of the mantle is linear or nonlinear?, *Geophys. Res. Lett.*, **22**, 1645–1648.
- Wu, P., 2002a. Mode coupling in a viscoelastic self-gravitating spherical earth induced by axisymmetric loads and lateral viscosity variations, *Earth planet. Sci. Lett.*, **202**, 49–60.
- Wu, P., 2002b. Effects of nonlinear rheology on degree 2 harmonic deformation in a spherical self-gravitating earth, *Geophys. Res. Lett.*, **29**, 10.1029/2001GL014109.
- Wu, P., 2002c. Effects of mantle flow law stress exponent on postglacial induced surface motion and gravity in Laurentia, *Geophys. J. Int.*, **148**, 676–686.
- Wu, P. & Peltier, W.R., 1982. Viscous gravitational relaxation, *Geophys. J. R. astr. Soc.*, **70**, 435–485.
- Wu, P., Ni, Z. & Kaufmann, G., 1998. Postglacial rebound with lateral heterogeneities: From 2D to 3D modeling, in *Dynamics of the Ice Age Earth: a Modern Perspective*, pp. 557–582, ed. Wu, P., Trans. Tech. Publ., Switzerland.
- Zhong, S. & Zuber, M.T., 2000. Long-wavelength topographic relaxation for self-gravitating planets and its implications to the compensation of lunar basins, *J. geophys. Res.*, **105**, 4153–4164.
- Zhong, S., Zuber, M.T., Moresi, L. & Gurnis, M., 2000. The role of temperature-dependent viscosity and surface plates in spherical shell models of mantle convection, *J. geophys. Res.*, **105**, 11 063–11 082.
- Zuber, M.T., Bechtel, T.D. & Forsyth, D.W., 1989. Effective elastic thicknesses of the lithosphere and mechanisms of isostatic compensation in Australia, *J. geophys. Res.*, **94**, 9353–9367.